https://doi.org/10.1016/j.tws.2022.109770


# Experimental and numerical investigations on stub column behaviour of cold-formed high strength steel irregular octagonal hollow sections

Jun-zhi Liu[1]; Han Fang[2]; Tak-Ming Chan[3,4] *

[1] School of National Safety and Emergency Management, Beijing Normal University, Beijing, China.
(Formerly, Department of Civil and Environmental Engineering, The Hong Kong Polytechnic University, Hong Kong, China)
[2] School of Civil Engineering, University of Leeds, United Kingdom.
(Formerly, School of Civil, Environmental and Mining Engineering, The University of Adelaide, South Australia 5005, Australia)
[3] Department of Civil and Environmental Engineering, The Hong Kong Polytechnic University, Hong Kong, China.
[4] Chinese National Engineering Research Centre for Steel Construction (Hong Kong Branch), The Hong Kong Polytechnic University, Hong Kong, China.
* Corresponding author: tak-ming.chan@polyu.edu.hk

## Abstract

Comprehensive experimental and numerical investigations into the structural behaviour of cold-formed high-strength steel (HSS) irregular octagonal hollow sections (IOctHS) are presented in this paper. A total of 13 IOctHS stub columns were tested. Material properties measurements were conducted on the tensile coupons taken from both parent plates and within the cross-sections of HSS IOctHS stub columns. Initial local geometric imperfection measurements were also carried out. In conjunction with experimental tests on the stub columns, finite element (FE) models were developed to replicate the test results and failure modes. Afterwards, the validated FE models were employed to conduct parametric studies to supplement the experimental data by generating further structural performance data covering a broader range of cross-section slenderness. Cross-section slenderness limits set out in design codes such as EN 1993-1-1, ANSI/AISC 360-16, AS 4100 as well as ASCE/SEI 48, and design methods of DSM as well as CSM were evaluated against the experimental and numerical data. It was found that the current limits for internal compression plate elements of rectangular hollow sections set out in the design standards are not suitable for the design of cold-formed HSS IOctHS under compression load. Cross-section strength predictions obtained from EN 1993-1-12, ANSI/AISC 360-16, AS 4100, ASCE/SEI 48, DSM, CSM and modified design methods were also compared with the tests and numerical results. Relatively accurate predictions are provided by design codes. Non-conservative results are obtained from DSM and the CSM yields more consistent and precise results than DSM. The modified design approaches were also assessed and discussed.

**Keywords:** High strength steel; Local buckling behaviour; Irregular octagonal sections; Material properties; Numerical modelling; Design methods.

## 1. Introduction

The advancement of the high-strength steel (HSS) technology promotes the extensive applications of HSS in large-scale and high-rise buildings due to the comparably high strength-to-weight ratio as well as the low carbon footprint, resulting in lighter structural components with smaller dimensions compared with normal strength steel (NSS) [1-2]. Structural hollow sections, also known as tubular sections, exhibit numerous advantages such as the great structural efficiency, higher torsional resistance than open sections as well as the

possibility for concrete infill as composite structures. HSS hollow sections integrate the merit of hollow sections and HSS materials to increase the benefits. Numerous experimental investigations on tubular sections fabricated using different processes have been conducted in the past years. It is a common method to fabricate the hollow sections by welding the HSS plate elements separately, and sections fabricated using this method are known as the welded (built-up) hollow sections. The behaviour of welded box sections concerning the local buckling performance has been investigated [3-6]. In addition to the welded sections, cold-formed HSS sections are also available in the market with the technological advancement. Compared with the welded sections, cold-formed sections feature the advantages such as easier fabrication, less energy consumption and relatively higher cross-section capacities due to the strength enhancements with cold-forming effect. Experimental investigation for HSS cold-formed sections have been performed to study the local buckling behaviour of the HSS hollow sections with square (SHS), rectangular (RHS) and circular (CHS) shapes [7-9]. Moreover, investigations on local buckling behaviour for hot-finished HSS hollow sections have also been carried out by Fang and Chan [10], Wang et al. [11] and Gkantou et al. [12].

Compared with conventional profiled steel as well as tubular components such as RHS/SHS or CHS, octagonal (OctHS) and irregular hollow sections (IOctHS) have attracted researchers' attention [13-21]. Specifically, the flat surfaces provided by OctHS/IOctHS allow for easier connection construction with incoming members as an operation platform, compared with CHS. The better local buckling resistance in comparison with the RHS/SHS have been demonstrated in previous studies [14, 17]. Moreover, the IOctHS with increased depth of the web of the OctHS becomes a solution to increase the major-axis stiffness of the cross section in bending for beam or beam-column members. The application of irregular octagonal sections also facilitates the development of modular integrated construction, which provide versatility of the structural configurations and connection options. Furthermore, the composite members formed with infill concrete can be employed as the primary column in high-rise buildings. For instance, the mega columns in high-rise buildings employ the hexagonal sections to connect the chord and frame [22, 23] which further elucidate the potential application of IOctHS in structural construction. Experimental investigations on the residual stresses distribution and material properties variations of HSS irregular octagonal hollow sections (IOctHS) have been carried out in Liu et al. [19]. Nevertheless, no experimental investigation on local buckling behaviour of HSS cold-formed irregular octagonal sections was performed.

Up to now, design specifications for HSS OctHS and IOctHS are not given in structural steel design codes including EN 1993-1-12 [24], AISI/AISC 360-16 [25] and AS 4100 [26]. Cross-section classification and cross-section strength design for OctHS are given in ASCE/SEI 48-16 [27]. The applicability of these design specifications to HSS IOctHS needs to be evaluated. Well-understanding of the interactions between the constituent plates comprising IOctHS for accurate strength predictions is necessary for the application and analysis for IOctHS. This study therefore presents the experimental and numerical investigations on local buckling behaviour of the HSS cold-formed IOctHS stub columns. A comprehensive experimental programme was performed on thirteen HSS cold-formed IOctHS stub columns with a larger spectrum of cross-section slenderness ($b_L/t$) varying from 8.3 to 38.2. Tensile coupon specimens were extracted within the cross sections of each stub column specimen and tested to obtain the tensile properties. Distributions of the initial local geometric imperfections were also measured before the implementation of the stub column tests. Further to the stub column tests, non-linear finite element (FE) models were developed to simulate the cold-formed steel HSS IOctHS under compressive load and validated using the obtained experimental results and failure modes. The validated numerical models were further used in the parametric study to investigate the cross- section

behaviour with a wider range of cross section geometries. The stub column cross-section strengths obtained from the stub column tests and parametric studies were subsequently used to assess the existing design codes, and the predicted cross-sectional resistance from design methods of Direct Strength Method (DSM) [28], Continuous Strength Method (CSM) [29] and modified DSM and CSM [18]. The accuracy of strength predictions based on these methods was discussed.

## 2. Test specimens

### 2.1 General

A total of 13 HSS IOctHS stub column specimens were employed in the experimental tests. HSS plates with nominal thicknesses of 6 mm and 10 mm were used to fabricate the HSS IOctHS in this study. The cold-formed HSS IOctHS in this study were fabricated by welding two half-sections with gas metal arc welding (GMAW) in longitudinal direction. During the welding process, the current $I$ was varied between 120 A and 130 A, while the voltage $U$ was between 19 V and 21 V and the welding velocity $v$ was about 120 mm/min, resulting in linear heat input ranging between 0.90 kJ/mm and 1.09 kJ/mm. The thermal efficiency coefficient $k$ is taken as 0.8 for GMAW [2, 22]. Each half-section was featured with four cold-bent corners through press-braking processes, as shown in Fig. 1. To have an over-matched welding condition, 1.2 mm electrode of ER110S-G category ($f_y$ = 860 MPa, $f_u$ = 920 MPa) was selected. The measured dimensions of the specimens are presented in Table 1 using the symbols defined in Fig. 2. The detailed definition of the symbols of the cross section are demonstrated in Fig. 3, where $H$ is the height of the cross section, $B_L$ is the long edge length of the IOctHS, $B_s$ is the short edge length, $b_L$ is the clear width of the longer flat portion with welding bead excluding the corner regtions, $b_s$ is the clear width of an inclined short flat side excluding the corner portions, $t$ is the nominal thickness of the cross section, $r_o$ and $r_i$ are the outer and inner corner radius of the cross section. It should be noted that the thickness $t$ was measured at the end section with a digital Vernier caliper at the locations shown in Fig. 4(a). Since the thickness measurement along the specimen length at mid portions was not accessible, an ultrasonic measurement gauge was used with the measured points as shown in Fig. 4(b). The measured data were averaged and summarized in Table 1. A labelling system is employed in this study to identify the specimen with its dimensions. The specimens were labelled in a form of "IOctHS nominal edge length $B_L$ × thickness-aspect ratio". Taking specimen of IOctHS185×6-2.00# as an example, the label represents that the specimen was fabricated with nominal $B_L$ of 185 mm, nominal $t$ of 6 mm and the aspect ratio of 2.0. The "#" symbol indicates that it is a repeated test specimen.

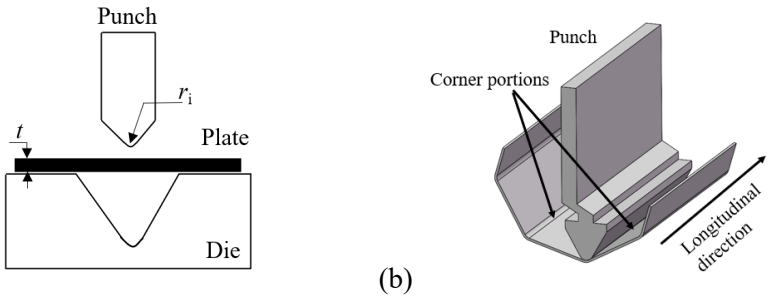


Fig. 1. Manufacturing process of press-braking (a) schematic view of press-braking (b) press-braking for HSS cold-formed IOctHS stub column.

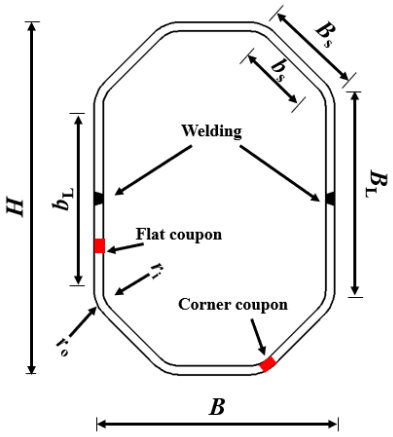


Fig. 2. Cross section of the HSS cold-formed irregular octagonal hollow section.

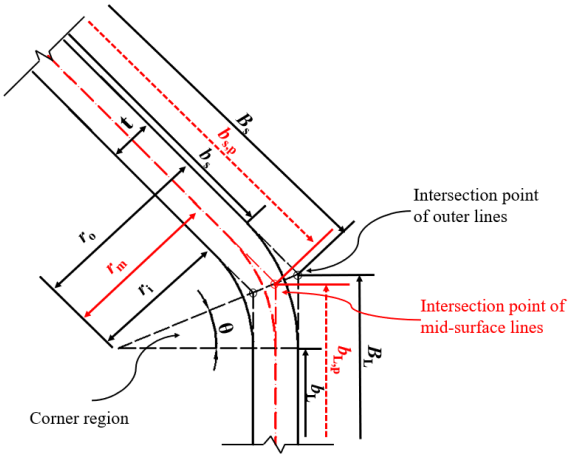


Fig. 3. Cross section of the HSS cold-formed irregular octagonal hollow section.

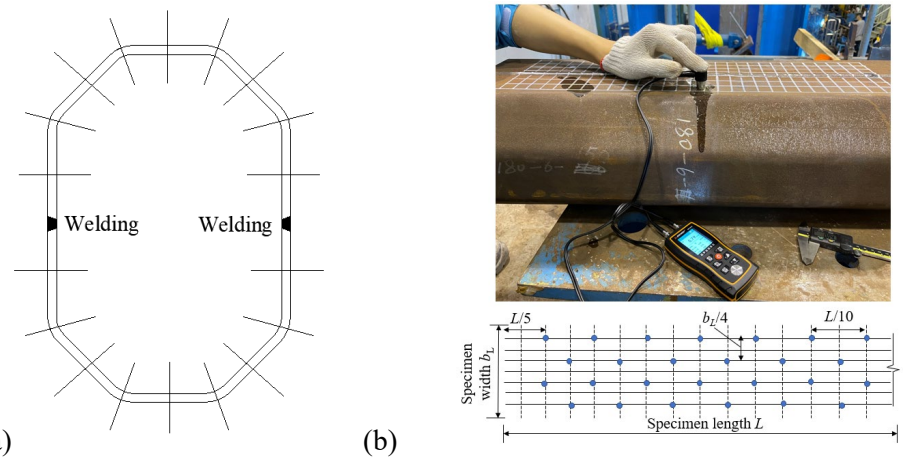


(a) (b)

Fig. 4. Measurements of the thickness of HSS cold-formed irregular octagonal hollow section (a) Thickness measurements at the end of the cross-section of specimen (b) Testing arrangement of thickness measurement using an ultrasonic gauge.

.

Table 1 Measured geometric dimensions and initial local geometric imperfections of HSS IOctHS stub column specimens.

| Section | Edge length $B_s$ (mm) | Side width $b_s$ (mm) | Edge length $B_L$ (mm) | Side width $b_L$ (mm) | Depth $H$ (mm) | Thickness $t$ (mm) | Length $L$ (mm) | Inner radius $r_i$ (mm) | $b_s/t$ (-) | $b_L/t$ (-) | Area $A$ ($mm^2$) | $\omega_0$ (mm) |
|---|---|---|---|---|---|---|---|---|---|---|---|---|
| IOct70×6-1.25 | 41.1 | 21.6 | 68.7 | 49 | 126.8 | 5.89 | 350 | 18.0 | 3.7 | 8.3 | 2159.7 | 0.25 |
| IOct145×6-1.25 | 91.2 | 71.0 | 145.7 | 125.3 | 274.6 | 5.88 | 655 | 18.0 | 12.1 | 21.3 | 4862.1 | 0.33 |
| IOct145×6-1.25# | 91.1 | 70.5 | 145.1 | 125.1 | 271.2 | 5.90 | 655 | 18.0 | 11.9 | 21.2 | 4811.2 | 0.35 |
| IOct145×6-1.50 | 66.3 | 46.6 | 144.4 | 124.5 | 288.4 | 5.91 | 575 | 18.0 | 7.9 | 21.1 | 3961.5 | 0.38 |
| IOct165×6-1.50 | 75.6 | 55.6 | 164.9 | 145 | 271.7 | 5.88 | 655 | 18.0 | 9.5 | 24.7 | 4535.1 | 0.65 |
| IOct185×6-1.50 | 85.8 | 65.9 | 183.4 | 163.5 | 304.7 | 5.89 | 735 | 18.0 | 11.2 | 27.8 | 5124.3 | 0.71 |
| IOct185×6-1.50# | 85.6 | 65.5 | 183.2 | 163.1 | 304.1 | 5.88 | 735 | 18.0 | 11.1 | 27.7 | 5121.2 | 0.86 |
| IOct205×6-2.00 | 61.5 | 41.5 | 205.9 | 186.0 | 292.8 | 5.90 | 705 | 18.0 | 7.0 | 31.5 | 4519.5 | 0.91 |
| IOct225×6-2.00 | 67.6 | 47.6 | 224.4 | 204.5 | 319.9 | 5.90 | 900 | 18.0 | 8.1 | 34.7 | 4961.1 | 0.95 |
| IOct245×6-2.00 | 73.2 | 53.2 | 246.4 | 224.4 | 349.8 | 5.88 | 850 | 18.0 | 9.0 | 38.2 | 5426.7 | 1.12 |
| IOct145×10-1.50 | 69.9 | 36.8 | 146.2 | 113.1 | 245.1 | 9.85 | 575 | 30.0 | 3.7 | 11.5 | 6668.1 | 0.45 |
| IOct145×10-1.50# | 69.7 | 36.5 | 145.8 | 112.6 | 244.8 | 9.84 | 575 | 30.0 | 3.7 | 11.4 | 6659.5 | 0.48 |
| IOct185×10-2.00 | 58.9 | 26.0 | 185.4 | 152.3 | 269.1 | 9.88 | 635 | 30.0 | 2.6 | 15.4 | 6805.1 | 0.51 |

Note: # indicates the repeated test specimen

## 2.2 Material properties measurements

Tensile coupon tests were conducted on coupon specimens extracted from the parent plates and HSS IOctHS to determine the material properties. An in-house electromechanical high force universal testing system of Instron 5982 testing machine with a capacity of 100 kN was used to conduct the tensile coupon tests. The dimensions of the coupon specimens were carefully designed in accordance with EN 6892-1: 2019 [30]. An optical non-contact video extensometer was used to capture the full engineering stress-strain relationship by painting the two customized white dots within the gauge length of either 25 mm or 50 mm depending on the coupon specimen geometries. The obtained stress-strain curves were used to determine the yield strength and ultimate strength as well as other material properties. The material properties for parent plates were firstly measured and are presented in Table 2, where $E_{s,p}$ indicates the elastic modulus of the parent steel plate, $f_{y,p}$ is yield strength, $f_{u,p}$ is the ultimate strength, $\varepsilon_{sh,p}$ is strain-hardening strain, $\varepsilon_{u,p}$ is strain at ultimate strength, $\varepsilon_{f,p}$ is elongation at fracture.

Material properties at two critical locations, namely the flat and the corner portions, for all HSS IOctHS specimens were determined by testing the flat and corner coupons. The flat coupon specimens were machined with 4 mm and 8 mm width along the gauge length respectively for those from the sections with plate thicknesses of 6 mm and 10 mm. The test arrangement of the tensile coupon is shown in Fig. 5. For each corner coupon, two holes with diameter of 10 mm were drilled at the distance of 20 mm from the end of the coupon, as verified according to EN 1993-1-8 [31]. A pair of specially developed grips with two pins was utilized to apply the tensile load through its centroid, as shown in Fig. 5. Detailed testing procedure was described in the previous study [19] on material properties variations. The measured material properties of the flat and corner coupons are tabulated in Table 3 and Table 4 respectively. The letter "f" in subscript in Table 3 indicates that the material properties are from flat coupon specimens whereas the letter "c" indicates the material properties are derived from the corner coupon specimens. Measured stress-strain curves for parent coupons are plotted in Figs 6–7 while typical measured stress-strain curves for the flat coupon and corner coupon taken from the section of IOct205×6-2.00 are shown in Fig. 8. Due to the cold-formed effect, corner coupons featured higher yield strength and ultimate strength but lower elongation of fracture and ultimate strain.

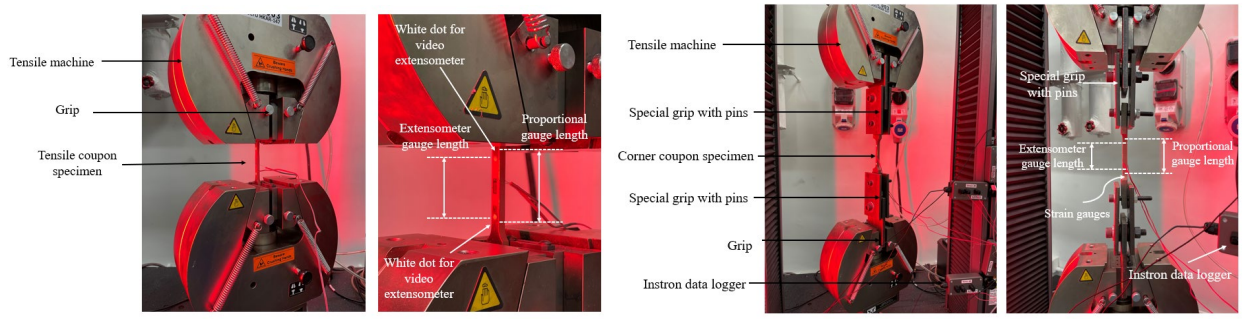


(a) (b)

Fig. 5. Test set-up for tensile coupon tests on (a) flat coupon specimens (b) corner coupon specimens [19].

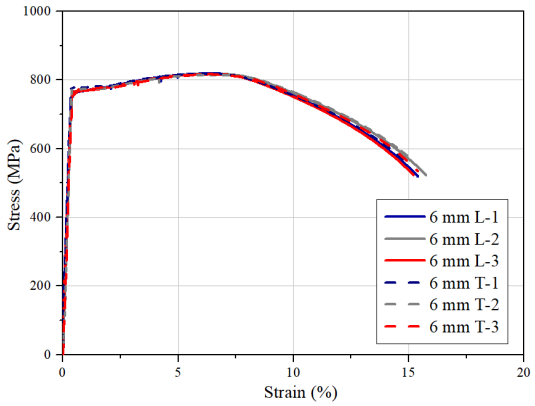


Fig. 6. Measured material stress-strain curves of Q690 high strength steel longitudinal and transverse tensile coupons extracted from 6 mm thick parent plate ("L" indicates the longitudinal direction and "T" indicates the transverse direction) [22].

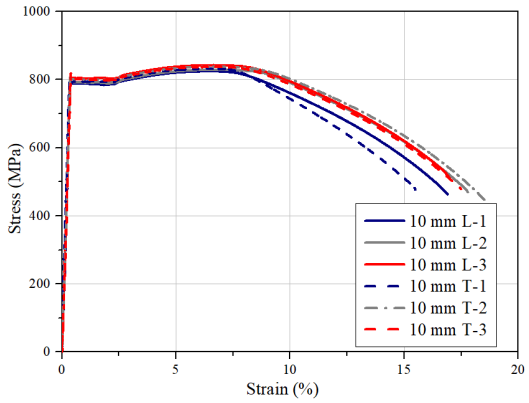


Fig. 7. Measured material stress-strain curves of Q690 high strength steel longitudinal and transverse tensile coupons extracted from 10 mm thick parent plate ("L" indicates the longitudinal direction and "T" indicates the transverse direction) [22].

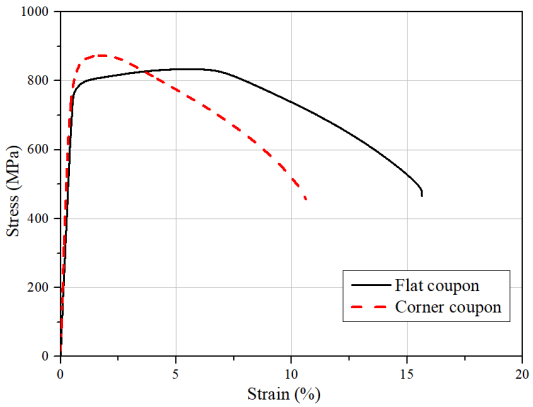


Fig. 8. Typical measured material stress-strain curves for tensile coupons extracted from HSS IOctHS stub column of IOct205×6-2.00.

Table 2 Mean test results of the flat coupons taken from the HSS parent plates.

| Section | $E_{s,p}$ (GPa) | $v$ | $f_{y,p}$ (Mpa) | $f_{u,p}$ (Mpa) | $\varepsilon_{u,p}$ (%) | $\varepsilon_{f,p}$ (%) | $\varepsilon_{sh,p}$ (%) |
|---|---|---|---|---|---|---|---|
| 6 mm plate | 214.1 | 0.29 | 768.5 | 816.2 | 6.45 | 14.95 | 1.98 |
| 10 mm plate | 216.1 | 0.30 | 791.3 | 825.6 | 6.55 | 16.18 | 2.32 |

Table 3 Test results of the material properties of the flat coupons taken from the sections.

| Section | $E_{s,f}$ (GPa) | $f_{y,f}$ (MPa) | $f_{u,f}$ (MPa) | $\varepsilon_{u,f}$ (%) | $\varepsilon_{f,ex,f}$ (%) | $\varepsilon_{f,f}$ (%) | $f_{0.05,f}$ (MPa) |
|---|---|---|---|---|---|---|---|
| IOct70×6-1.25 | 221.3 | 785 | 832 | 6.2 | 15.8 | 15.5 | 778 |
| IOct145×6-1.25 | 221.4 | 780 | 827 | 5.8 | 16.1 | 16.0 | 780 |
| IOct145×6-1.50 | 212.1 | 782 | 838 | 6.3 | 14.5 | 16.2 | 775 |
| IOct165×6-1.50 | 213.4 | 781 | 829 | 6.2 | 15.6 | 15.2 | 771 |
| IOct185×6-1.50 | 219.3 | 776 | 828 | 6.4 | 15.1 | 15.5 | 770 |
| IOct205×6-2.00 | 216.2 | 783 | 836 | 6.6 | 16.2 | 16.0 | 778 |
| IOct225×6-2.00 | 202.5 | 788 | 840 | 6.3 | 15.7 | 15.6 | 768 |
| IOct245×6-2.00 | 212.3 | 780 | 829 | 6.4 | 15.8 | 15.7 | 776 |
| IOct145×10-1.50 | 217.5 | 800 | 836 | 6.9 | 18.9 | 18.2 | -* |
| IOct185×10-2.00 | 196.5 | 803 | 834 | 5.5 | 15.6 | 15.8 | 760 |

Table 4 Test results of the material properties of the corner coupons taken from the sections.

| Section | $E_{s,c}$ (GPa) | $f_{y,c}$ (MPa) | $f_{u,c}$ (MPa) | $\varepsilon_{u,c}$ (%) | $\varepsilon_{f,ex,c}$ (%) | $\varepsilon_{f,c}$ (%) | $f_{0.05,c}$ (MPa) |
|---|---|---|---|---|---|---|---|
| IOct70×6-1.25 | 206.2 | 820 | 853 | 3.5 | 10.6 | 11.2 | 780 |
| IOct145×6-1.25 | 204.6 | 802 | 849 | 1.5 | 9.9 | 10.5 | 650 |
| IOct145×6-1.50 | 196.7 | 800 | 854 | 1.9 | 12.7 | 12.4 | 720 |
| IOct165×6-1.50 | 205.0 | 800 | 850 | 1.6 | 9.6 | 10.2 | 680 |
| IOct185×6-1.50 | 197.1 | 798 | 841 | 1.8 | 10.6 | 10.3 | 650 |
| IOct205×6-2.00 | 208.4 | 804 | 870 | 1.5 | 10.4 | 11.0 | 686 |
| IOct225×6-2.00 | 195.5 | 815 | 860 | 1.4 | 11.2 | 11.5 | 765 |
| IOct245×6-2.00 | 186.9 | 808 | 849 | 2.5 | 10.7 | 11.2 | 740 |
| IOct145×10-1.50 | 213.3 | 830 | 890 | 1.8 | 12.6 | 12.2 | 718 |
| IOct185×10-2.00 | 193.4 | 818 | 871 | 1.6 | 12.6 | 11.8 | 756 |

## 2.3 Geometric imperfection measurements

Local geometric imperfections are inevitably introduced into structural elements during manufacturing, transportation, and installation. It affects the structural responses such as onset of local buckling, initiation of the plasticity and ultimate resistance strength. The initial local geometric imperfections were measured for each HSS IOctHS stub column prior to the testing of the specimens. A set of three Linear Variable Displacement Transducers (LVDTs) with an accuracy of 0.001 mm was used and affixed to the head of the milling machine using a specially developed fixture which can move longitudinally along the length of the specimen. Fig. 9 shows the test set-up and the Linear Variable Displacement Transducers (LVDTs) arrangement of the measurement as well as the sign convention of the measured local imperfection. The similar set-ups were also successfully applied by Chen et al. [32] and Liu et al. [33, 34]. The specimens were placed on a milling machine as a measurement platform. Each surface of the specimens was measured with two LVDTs located near the corner of the section and one at the mid portion of the flat portion. To eliminate the possible local imperfection caused by cold sawing, the measurements were started and terminated at the location 50 mm away from each end of the specimen [7, 23]. The data was measured and recorded at a 2 mm interval along the specimen length. The local geometric imperfection was derived as the deviation between the measurement at the mid-portion and a straight datum line connecting the measurements at the corners. The measured maximum amplitude of the local geometric imperfection for each specimen is reported in Table. 1.

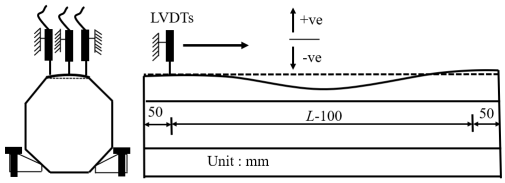


(a) Schematic view

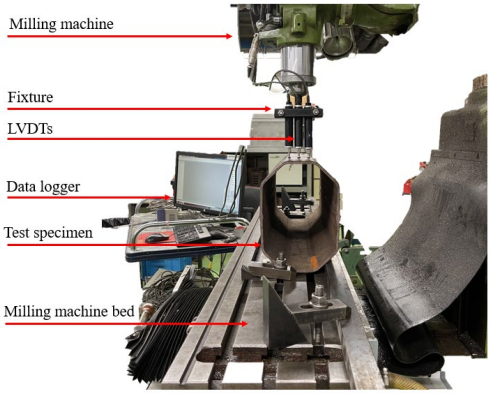


(b) Experimental arrangement

Fig. 9. Set-up of the local geometric imperfection measurement for HSS IOctHS stub columns.

## 3. Stub column tests

Concentric compressive tests on 13 stub columns were carried out to investigate the structural response at the cross-sectional level including the local buckling behaviour and the resistance under compression. The stub column tests were conducted at the Structural Engineering Research Laboratory at The Hong Kong Polytechnic University. The nominal length of the stub columns was carefully designed for each cross section to avert the occurrence of global buckling in accordance with the rule that the length of specimens was determined within 20 times the least radius of gyration [35]. Moreover, the section should be sufficiently long to contain the representative pattern of local geometric imperfection and residual stresses. The non-dimensional member slenderness $\bar{\lambda} = (Af_y/N_{cr})^{0.5}$ was designed for all specimens with magnitude of 0.12, which was far below than the threshold magnitude of 0.2 for global buckling. Note that $N_{cr}$ is the elastic critical buckling load for column member. To ensure a uniform distribution of the compressive stress over the cross section, the specimens' ends were milled flat so that the end plates can contact well with specimens for uniform loading. The compressive loading test was conducted by using a universal servo-controlled testing machine with a capacity of 25000 kN.

The test set-up and instrumentation are shown in Figs. 10(a)–10(b). The stub column specimens were loaded between the two parallel hardened end plates. The hardened plate was used between the end of the specimens and the machine to avoid damage due to the high localized stress. Moreover, a pair of specially developed end clampers (end stiffeners) comprising numerous high strength bolts with height of 30 mm were stiffened to the specimens to prevent premature of the failure near the ends of the specimens, as shown in Fig. 10(a). A spherical bearing on the top of the end plate was used to eliminate the gap, if any, between the specimens and the bearing plate. Furthermore, four 50 mm range Linear Variable Displacement Transducers (LVDTs) were used to measure the end shortening of the stub columns. An initial load of approximately 20.0 kN was applied to the specimens by which any possible gaps between the specimen and the bearing plate can be eliminated. All the stub column test specimens were compressed at a constant loading speed of 0.05%$L$ mm/min, which is similar to the loading speed of the coupon specimens at the initial stage. In addition, a total of 12 strain gauges were attached on each specimen at the mid-height to determine the axial strain and detect the initiation of local buckling. The arrangement of the location of the strain gauges was carefully designed to sufficiently reflect the differences of material properties across the section. Moreover, the readings from the strain gauges were utilized to modify the initial stage of the LVDT readings, removing the effect of the initial gaps and the elastic deformation from the end plates, by which true specimen end shortening can be derived.

The obtained test results are normalized to the squash load of $N_y$. It should be noticed that the yield load $N_y = A \times f_{y,m}$ where $f_{y,m}$ is the average yield strength weighted by the area of flat regions and corner regions for cold-formed sections. The normalized axial load-end shortening responses for HSS IOctHS specimens are plotted in Fig. 11. Key experimental results of the IOctHS stub column tests including the ultimate axial load $N_u$, the end shortening at ultimate load $\delta_u$, yield load $N_y$ and the ultimate to yield load ratio $N_u/N_y$ are summarized in Table 5. Moreover, the comparisons between the test results and the predicted bearing capacities from numerous design codes and design approaches with statistical analysis results are also presented. Failed specimens with representative local buckling failure modes are shown in Fig. 12. Those sections with normalized ratio of $N_u/N_y$ larger than unity were able to reach yield load whereas for the sections failed before reaching plastic load are failed due to local buckling with $N_u/N_y$ lower than the unity. For the stub column specimens failed by cross-section yielding, such as the specimen of IOct70×6-1.25, IOct145×10-1.50, and IOct185×10-2.00, comparably larger normalized cross-section resistance and deformation are observed. For those sections failed by local buckling prior to the attainment of yield load, sharp drop in terms the load and lower deformation are observed. In terms of the comparisons between the design codes and design methods

against the experimental results, relatively accurate and consistent results are provided from the design codes of EN 1993-1-12, ANSI/AISC 360-16, AS 4100, ASCE/SEI 48 with the mean values of $N_u/N_{,pred}$ equals to 0.99, 0.99, 1.00 and 0.99 respectively and the corresponding CoVs are 0.081, 0.085, 0.070 and 0.089. For the investigated test specimen, the strength predictions from DSM provide more accurate results than CSM though the predicted data are largely scattered.

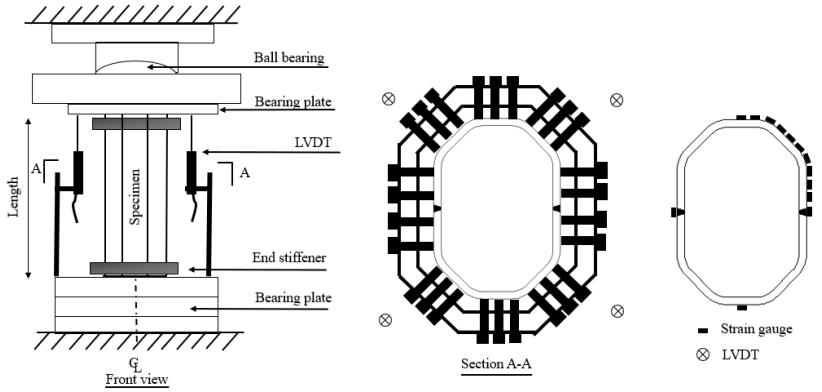


(a) Schematic view of the test set-up and the end clamper


(b) Experimental set-up

Fig. 10. Test set-up for HSS cold-formed IOctHS stub column.

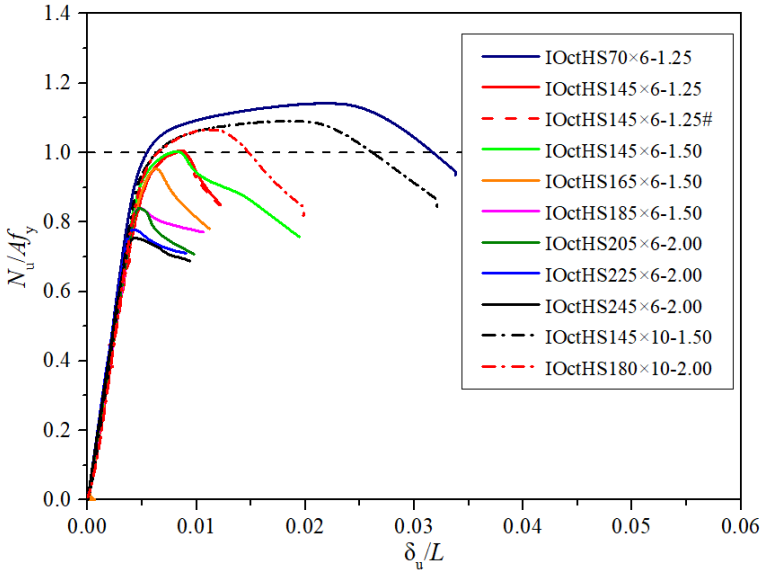


Fig. 11. Normalized load-end shortening curves of the cold-formed HSS IOctHS stub columns.

Fig. 12. Experimental failure modes of the representative cold-formed HSS IOctHS stub columns.

Table 5 Summary of HSS cold-formed IOctHS stub column test results.

| Specimens | $N_{u,test}$ (kN) | $\delta_u$ (mm) | $N_{u,test}$ /$Af_y$ | $N_{u,test}$ / $N_{u,EC3}$ | $N_{u,test}$ /$N_{u,AISC}$ | $N_{u,test}$ /$N_{u,AS4100}$ | $N_{u,test}$ / $N_{u,DSM}$ | $N_{u,test}$ / $N_{u,CSM}$ | $N_{u,test}$ / $N_{u,DSM}^{*}$ | $N_{u,test}$ / $N_{u,CSM}^{*}$ | $N_{u,test}$ / $N_{u,ASCE}$ | $N_{u,test}$ / $N_{u,Fang}$ | $N_{u,test}$ / $N_{u,ASCE}^{*}$ | $N_{u,test}$ / $N_{u,ASCE}^{\#}$ |
|---|---|---|---|---|---|---|---|---|---|---|---|---|---|---|
| IOct70×6-1.25 | 1874 | 7.90 | 1.13 | 1.14 | 1.14 | 1.14 | 1.14 | 1.10 | 1.14 | 1.04 | 1.14 | 1.14 | 1.14 | 1.14 |
| IOct145×6-1.25 | 3696 | 3.55 | 0.99 | 1.01 | 1.01 | 1.01 | 1.01 | 1.01 | 1.05 | 1.05 | 1.01 | 1.04 | 1.04 | 1.10 |
| IOct145×6-1.25# | 3676 | 3.51 | 0.99 | 1.00 | 1.00 | 1.00 | 1.00 | 1.01 | 1.05 | 1.05 | 1.00 | 1.03 | 1.03 | 1.10 |
| IOct145×6-1.50 | 3024 | 2.98 | 0.99 | 1.00 | 1.00 | 1.00 | 1.00 | 1.00 | 1.04 | 1.04 | 1.00 | 1.04 | 1.04 | 1.02 |
| IOct165×6-1.50 | 3275 | 2.72 | 0.94 | 0.99 | 0.97 | 0.98 | 1.01 | 1.09 | 1.12 | 1.12 | 0.96 | 1.02 | 1.02 | 1.00 |
| IOct185×6-1.50 | 3310 | 2.81 | 0.84 | 0.90 | 0.89 | 0.91 | 0.90 | 0.97 | 1.00 | 1.00 | 0.90 | 0.93 | 0.94 | 1.02 |
| IOct185×6-1.50# | 3311 | 2.78 | 0.84 | 0.91 | 0.90 | 0.92 | 0.90 | 0.98 | 1.00 | 1.00 | 0.91 | 0.94 | 0.94 | 1.03 |
| IOct205×6-2.00 | 2863 | 2.72 | 0.82 | 0.94 | 0.93 | 0.97 | 0.95 | 1.03 | 1.04 | 1.04 | 0.95 | 0.98 | 0.98 | 0.94 |
| IOct225×6-2.00 | 2929 | 2.82 | 0.77 | 0.90 | 0.89 | 0.94 | 0.93 | 1.02 | 1.03 | 1.03 | 0.83 | 0.94 | 0.94 | 0.90 |
| IOct245×6-2.00 | 3055 | 2.85 | 0.73 | 0.89 | 0.89 | 0.93 | 0.95 | 1.04 | 1.04 | 1.04 | 0.93 | 0.93 | 0.94 | 0.89 |
| IOct145×10-1.50 | 5544 | 9.55 | 1.05 | 1.09 | 1.09 | 1.09 | 1.09 | 1.07 | 1.09 | 1.05 | 1.09 | 1.09 | 1.09 | 1.17 |
| IOct145×10-1.50# | 5536 | 9.52 | 1.05 | 1.09 | 1.09 | 1.09 | 1.09 | 1.08 | 1.09 | 1.05 | 1.09 | 1.09 | 1.09 | 1.17 |
| IOct185×10-2.00 | 5543 | 5.91 | 1.03 | 1.07 | 1.07 | 1.07 | 1.07 | 1.06 | 1.07 | 1.05 | 1.07 | 1.07 | 1.07 | 1.07 |
| | | | Mean | 0.99 | 0.99 | 1.00 | 1.00 | 1.04 | 1.06 | 1.04 | 0.99 | 1.02 | 1.02 | 1.04 |
| | | | CoV | 0.081 | 0.085 | 0.070 | 0.074 | 0.039 | 0.038 | 0.026 | 0.089 | 0.066 | 0.064 | 0.087 |

Note: # indicates the repeated test specimen

## 4. Numerical simulations

### 4.1 Finite element modelling

In addition to the experimental investigation, finite-element (FE) analysis using commercially available software package ABAQUS [36] was also performed to replicate the experimental test and simulate the structural behaviour of the HSS IOctHS under compressive loading. In order to generate complementary data with a relatively large range of the cross-section slenderness and capture the failure modes of the stub columns, the validated FE model should be developed for further parametric studies. For the purpose of developing the valid FE model, the measured cross-section geometric dimensions were used with full length of the investigated specimens. For mechanical properties, the measured stress-strain responses for the flat and the corner coupons were converted to true stress and plastic strain in accordance with the relationship shown in Eqs. (1) – (2). Plastic material model with isotropic hardening was used for modelling steel materials. To consider the strength enhancement during the cold-forming process, the increased strength was assigned to the corner portion of the FE model. It was found that the enhancement of the strength was not limited to the corner portion only, it can be extended to a certain distance away from the corner. The extended corner regions with a width of 1.5$t$ is appropriate for OctHS [17] which was also used in this study, as shown in Fig. 13.

$$\sigma_{\text{true}} = \sigma_{\text{eng}}(1+\varepsilon_{\text{eng}}) \tag{1}$$

$$\sigma_{\text{true}}^{\text{pl}} = \ln(1+\varepsilon_{\text{eng}}) - (\frac{\sigma_{\text{true}}}{E_{\text{s}}}) \tag{2}$$

where $\sigma_{eng}$ and $\varepsilon_{eng}$ are the engineering stress and engineering strain from tensile coupon tests, $E_s$ is Young's modulus obtained from the tests, and $\sigma_{true}$ and $\varepsilon_{true}^{pl}$ are the true stress and plastic strain.

In line with the boundary condition setup in experimental tests, fix-ended boundary conditions were simulated by restraining all degrees of freedom except for the axial translation at one end and release the axial displacement at the other end in longitudinal direction only, as shown in Fig. 14. Linear elastic buckling analysis was performed to obtain the lowest elastic buckling eigen mode under compression which was taken as the representative distributed profile of initial local geometric imperfection, as shown in Fig. 15. The buckling mode shape was then amplified by the measured initial local geometric imperfection. Non-linear analysis accounting for material and geometric non-linearities was subsequently conducted. The incremental displacement control was used by assigning the displacement in axial direction using RIKS step. To allow for large displacement analysis, the function of nonlinear geometric parameter (*NLGEOM) should be activated. A four-node shell element with reduced integration S4R, commonly used for predicting the structural response of steel hollow sections [37-39], was employed in this study. The mesh size of $B_s$/20 based on mesh convergence analysis which strike a good balance between the accuracy and the computational costs was used in this study, where $B_s$ is the edge length of the inclined short flat portion. Aside from the measured initial local geometric imperfections for IOctHS stub columns, imperfection sensitivity analysis was executed to determine the proper magnitude of the imperfection incorporated to the model, considering (i) the measured imperfection value $\omega_0$ (ii) $t$/10 (iii) $t$/50 (iv) $\omega_{Fang}$ predictive model for local imperfection of OctHS proposed in [14]. The predictive model is shown in Eq. (3).

$$\omega_{\text{Fang}} = 0.307\left(\frac{\sigma_{0.2}}{f_{\text{cr}}}\right)^{0.5} t \tag{3}$$

The fabrication processes of press-braking and welding result in residual stresses. The residual stresses in longitudinal direction are more influential in comparison with the residual stresses in transverse direction, which can be further decomposed into membrane residual stresses and bending residual stresses. The bending residual stresses were inherently reintroduced during the elastic stage of straightening the curved coupon specimen during tensile coupon tests. Thus, the bending residual stresses were essentially included in the stress-strain relationship from the coupon specimens. To account for the effect of the residual stresses on the structural response in the FE model, the membrane residual stresses were incorporated into the FE model with the magnitudes obtained from the predictive model proposed for HSS IOctHS in Liu et al. [19], as shown in Fig. 16. The largest tensile membrane residual stresses near the welding seam featured with the magnitude of $0.56f_{\text{y,p}}$, gradually decreased as distance increasing, and then changed to compressive stress with magnitude of $0.16f_{\text{y,p}}$ at the locations away from the welding seam. As the distance increases far away from the welding at about the second press-braking corner, tensile membrane residual stresses were observed with a smaller magnitude of $0.12f_{\text{y,p}}$. A typical membrane residual stresses distribution incorporated into the FE model for the HSS cold-formed IOctHS stub column specimen IOct185×6-1.50 is depicted in Fig. 17 with positive values indicating tensile membrane residual stress and negative values implying compressive membrane residual stress. To evaluate the impact of the membrane residual stress on the cross-section strength and the local buckling response of the stub column specimens, the FE model with or without inclusion of the membrane residual stressed were both developed and the corresponding results were compared to determine the necessities for incorporating the membrane residual stresses in FE model. It was found that membrane residual stress cause 2-3% difference in the ultimate capacity and the existence residual stress induces earlier yielding of the IOctHS under compression. The membrane residual stresses were thereby modeled in the further parametric studies.

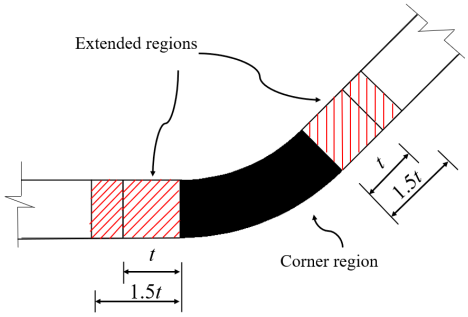


Fig. 13. Extension of the corner regions material properties in finite element model for cold-formed HSS IOctHS

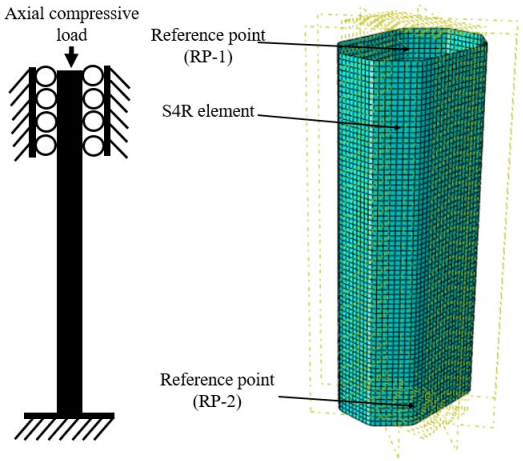


Fig. 14. Typical FE mesh, loading and boundary conditions of the cold-formed HSS IOctHS stub columns.

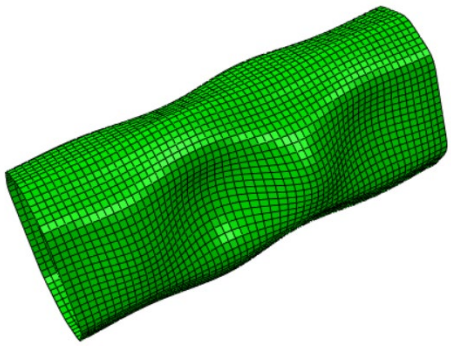

Fig. 15. Typical first buckling mode shape generated from Eigenvalue analysis.

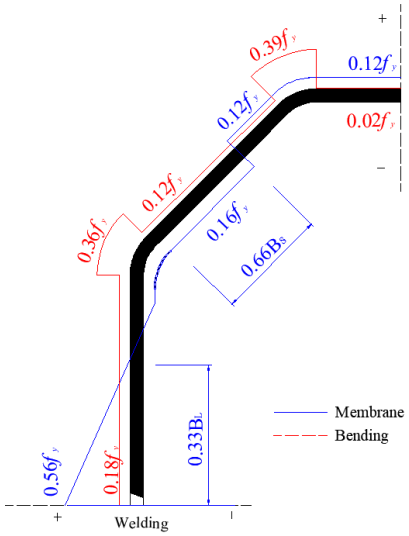


Fig. 16. Predictive model of membrane and bending residual stresses distributions and amplitudes (in MPa) in modelled cold-formed HSS IOctHS stub columns [19].

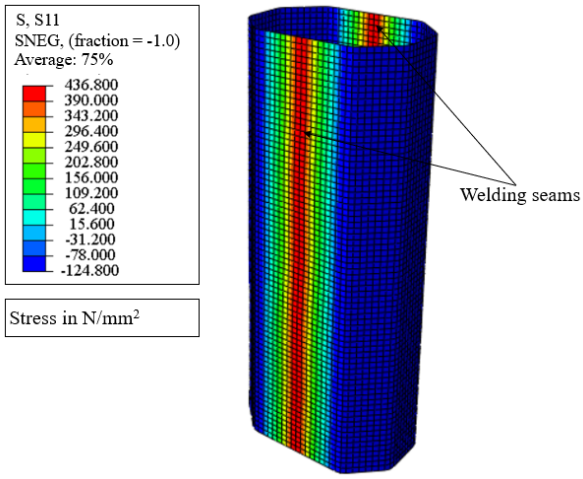


Fig. 17. Typical membrane residual stresses distributions in the modelled cold-formed HSS IOctHS stub columns of IOct185×6-1.50.

## 4.2 Validation of the FE models

The adequacy and accuracy of the FE models were elucidated by validation study through the comparisons of the failure mode, ultimate axial load, load-end shortening responses generated from FE models with those obtained from the tests. In Fig. 18, the failure modes of the HSS cold-formed IOctHS obtained from the numerical models were compared with that of the failed specimens. The failure modes generated from the FE model closely matched the test observations for IOctHS stub column specimens.

The axial load-end shortening curves of HSS cold-formed IOctHS stub columns of IOct70×6-1.25, IOct145×6-1.50 and IOct145×10-1.50 form FE models were compared with the counterparts obtained from the experimental tests. As seen in Fig. 19, the curves from experimental study correlate well with the numerical data and the ultimate capacities can be precisely captured. The sensitively analysis of the initial local geometric imperfection was performed by comparing the ultimate loads estimated from FE models incorporating different local imperfection amplitudes with those from the stub column tests, as presented in Table. 6. Mean values of the ratios of $N_{u,FE}/N_{u,test}$ for the four investigated initial local imperfection magnitudes are 1.02, 1.01, 1.05 and 1.04 respectively with corresponding CoVs of 0.018, 0.030, 0.038 and 0.027 respectively. The best agreement between the experimental and numerical predictions was achieved when the imperfection amplitude equals to $t/10$. This initial local imperfection value was thus used in the subsequent parametric studies. Overall, the developed FE models can accurately replicate the stub column test results in terms of ultimate loads, load-end shortening curves and failure modes.

## 4.3 Parametric studies

After the completion of the validation study for the developed FE models, parametric studies were carried out to further generate structural performance data with a larger range of cross-section slenderness aiming at complementing the experimental data. The average material properties from tensile coupon testing for flat coupons and corner coupons were used for the parametric studies. The stress-strain curves were generated based on the relationships given in Liu et al. [19] for materials at different regions and the material properties

were assigned to the corresponding locations of flat portions and corner portions. Concerning the initial local geometric imperfections, a value of $t/10$ is used as discussed in the sub-section of 4.2. In terms of the geometric dimensions, the clear width of the longer flat portion $b_L$ was varied from 46 mm to 170 mm, and clear width of the shorter inclined flat portion $b_s$ varied between 11 mm and 170 mm, resulting in a wider cross-section slenderness of $b_s$ varied between 1.9 and 28.8 and $b_L$ ranging between 8.3 and 28.8. The aspect ratio varied from 1.0 to 2.0 and the thickness of the plate was 6 mm. The outer corner radius and inner corner radius of the cold-bent corners were set to be $3t$ and $2t$ respectively. The length of the stub columns was determined in accordance with the principle introduced in section 3. A total of 150 FE models were conducted in the parametric studies. The experimental test data together with the generated FE results were used to assess and evaluate the applicability of the current structural steel design codes and the design methods.

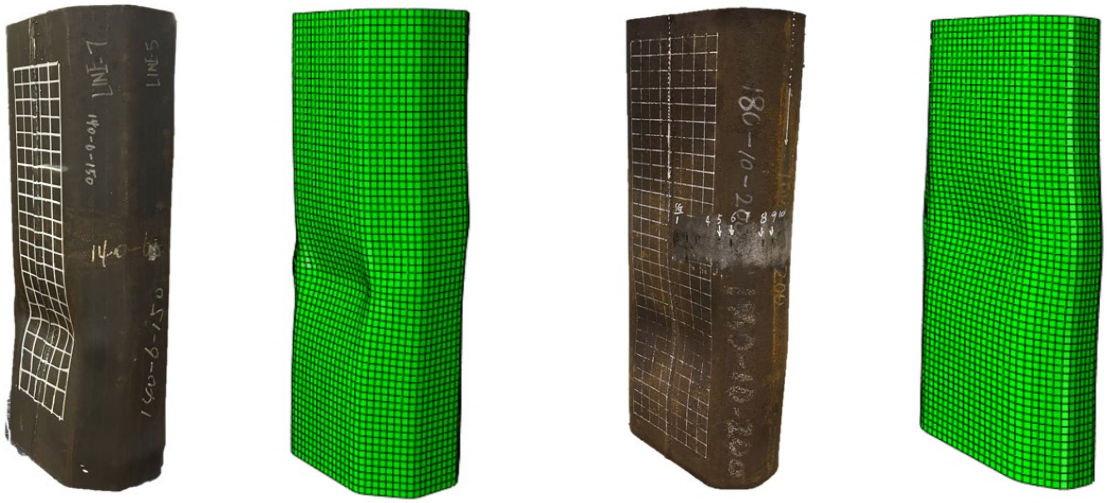

(a) (b)

Fig. 18. Test and FE failure modes for typical stub column specimens (a) Cold-formed HSS IOctHS stub column specimen IOct145×6-1.50 (b) Cold-formed HSS IOctHS stub column specimen IOct185×10-2.00.

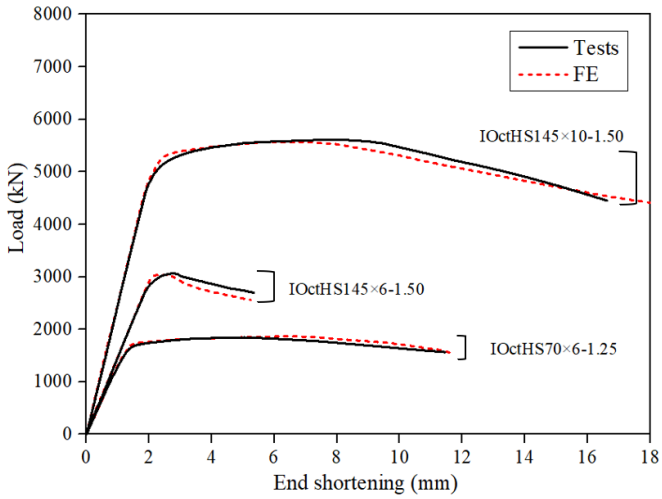


Fig. 19. Experimental and numerical load-end shortening responses for cold-formed HSS IOctHS stub columns.

Table 6 Comparison of the stub column test results with finite element results for various imperfection amplitudes.

| Specimens | $N_{u,FE}/N_{u,test}$ | | | |
|---|---|---|---|---|
| | $\omega_0$ | $t/10$ | $t/50$ | $\omega_{Fang}$ |
| IOct70×6-1.25 | 1.00 | 0.98 | 1.00 | 1.00 |
| IOct145×6-1.25 | 1.02 | 1.00 | 1.02 | 1.02 |
| IOct145×6-1.25# | 1.03 | 1.00 | 1.03 | 1.03 |
| IOct145×6-1.50 | 1.01 | 1.00 | 1.03 | 1.03 |
| IOct165×6-1.50 | 1.04 | 1.04 | 1.07 | 1.07 |
| IOct185×6-1.50 | 1.04 | 1.05 | 1.08 | 1.06 |
| IOct185×6-1.50# | 1.04 | 1.05 | 1.08 | 1.06 |
| IOct205×6-2.00 | 0.99 | 1.01 | 1.13 | 1.06 |
| IOct225×6-2.00 | 1.02 | 1.04 | 1.11 | 1.08 |
| IOct245×6-2.00 | 1.04 | 1.07 | 1.09 | 1.08 |
| IOct145×10-1.50 | 1.00 | 0.99 | 1.02 | 1.01 |
| IOct145×10-1.50# | 1.01 | 0.99 | 1.02 | 1.01 |
| IOct185×10-2.00 | 0.99 | 0.97 | 1.01 | 1.01 |
| Mean | 1.02 | 1.01 | 1.05 | 1.04 |
| CoV | 0.018 | 0.030 | 0.038 | 0.027 |

Note: # indicates the repeated test specimen

## 5. Evaluation of the current design codes and the design approaches

### 5.1 General

The applicability of the design provisions in the existing structural steel design codes for HSS IOctHS were evaluated and compared. It is worth noting that designs of OctHS or IOctHS are not included in current structural steel design standards such as EN 1993-1-12 [24], AISC 360-16 [25], AS 4100 [26], AISI S100-16 [40], and EN 1993-1-5 [41]. North American code of ASCE/SEI 48-11 [27] stipulates the design provisions for OctHS with slenderness limiting value provided. Previous study demonstrated that the plate buckling theory for the internal compression element in SHS/RHS can be applied to the internal plate members comprising OctHS with Q355 (nominal yield strength = 355 MPa) [42] and Q460 (nominal yield strength = 460 MPa) steel plates [17]. Hence, the specified limits for the internal plate element under compression regulated in the structural steel standards may be extended to cover the design of IOctHS. Note however that the design provisions in EN 1993-1-12 [24] stem from the design framework specified in EN 1993-1-1 [43] which covers the structural steel design with strength grade not greater than 460 MPa. The concept of the cross-section classification design is adopted in these design codes at cross-section level and the effective width method is widely used to deal with the members subject to local buckling. The modified design method based on the form of effective width method (EWM) equation set out in EN 1993-1-5 [41] was proposed in Fang et al. [14] for Q690 OctHS, and the suitability of this modified method coupled with the counterpart regulated in the codes were evaluated and compared. Apart from the design standards, design approaches including direct strength method (DSM) [28] and continuous strength method (CSM) [29] and the modified DSM* [18] which

can account for the interaction effect and can be applied to arbitrary cross-section shape were also assessed and discussed. Furthermore, the cross-section strengths obtained from the tests coupled with FE results were compared with the predicted strengths from these design standards and the design approaches.

### 5.2 Cross-section classification

Cross-section classification is the commonly used methodology for dealing with the cross section experiencing local buckling for the design of steel hollow sections including SHS, RHS, and CHS, as specified in European code of EN 1993-1-1 [43], ANSI/AISC 360-16 [25] and AS 4100 [26]. There are four cross-section classes specified in the classification framework of Eurocode EN 1993-1-1 [43]. For the cross-sections which can attain the yield of $Af_y$ are classified as Class 1, 2, and 3 sections, whereas those sections failed to achieve the yield load due to the occurrence of local buckling are categorized as Class 4. Likewise, cross-section classification is also specified in codes of ANSI/AISC 360-16 [25] and AS 4100 [26] but the number of the cross-section class is reduced to only two sections, namely non-slender or slender sections. Non-slender sections refer to the sections which can reach the yield load and slender sections indicate the sections that are failed due to local buckling prior to the attainment of the yield load. Thus, the slender sections can be considered as the corresponding class as Class 4 and non-slender sections are those sections corresponding to Class 1-3 in Eurocode 3. Though ASCE/SEI 48-11 [27] is not structural steel design standard, it also employs the classification system to apply for transmission pole design, which is similar as AISC 360-16 and AS 4100. To determine the cross-section slenderness, different material parameters are used in different design codes, such as $\varepsilon_{EC3} = (235/f_y)^{0.5}$, $\varepsilon_{AISC} = (E/f_y)^{0.5}$, and $\varepsilon_{AS4100} = (250/f_y)^{0.5}$ were used to account for the differences of the material strengths in various codes respectively. Note that in the design standard of AISI S100 [40] and AS/NZS 4600 [44], the parameter $\lambda_p$ is used as the cross-section slenderness, where $\lambda_p = (f_y/f_{cr})^{0.5}$. For the purpose of harmonized comparisons, the yield slenderness limits value are summarized in Table 7 in which a normalized plate slenderness value $\lambda_{lim} = (b/t)(f_y/E)^{0.5}$ is used to standardize the comparison between the codes and design methods. The normalized yield slenderness limits from EN 1993-1-1, AISC 360-16 and AS 4100 are similar with values of 1.405, 1.400, and 1.414 respectively, the slenderness limit value from ASCE/SEI 48-11 is relatively larger with $\lambda_{lim}$ of 1.520. Smaller slenderness limits are provided by AISI S100 and AS/NZS 4600 with a value of 1.280. Compression resistances from experimental and numerical investigations were used to normalize the corresponding squash load $Af_y$, and subsequently plotted against the ratios normalized plate slenderness $\lambda_{lim}$ of the governing plate member of the IOctHS in Fig. 20. The comparisons indicate that the current codified slenderness limits in these structural steel codes are inappropriate and cannot be extended to cover the design of HSS cold-formed IOctHS. In particular, the yield slenderness limits can hardly be applied to the sections with a larger aspect ratio of two. As can be seen in Fig. 20, the data points at upper bound are the sections with an aspect ratio of two, which benefit largely from the interaction effect with larger ratio of the normalized strength.

As discussed in the sub-section of 5.1 that EWM is used to explicitly consider the sections undergoing local buckling. The original dimension such as the width $b$ (slender member) of the cross-section is thus reduced to the effective width of $b_{eff}$ and the effective compressive resistance becomes at $A_{eff}f_y$, where $A_{eff}$ is the effective area of the section. Similarly, the other two steel design codes also specify the systematic classification and design system to consider the sections experiencing local buckling, though the expressions are different. The detailed discussion concerning EWM design in standards will be conducted in sub-section of 5.3. EN 1993-1-5 provides the slenderness limit of 1.279, almost same as the one in AISI S100. In the previous study on cross-

section resistance of OctHS in Fang et al. [14], modified cross-section slenderness limit was proposed. It was found that the proposed value of 1.00 can be safely adopted to cover the cross-section classification of IOctHS though relatively conservatism was observed for sections with aspect ratio larger than 1.0.

In addition to the design standards, design approaches such as DSM which is incorporated in the design code of AISI S100-16 [40], can be applicable to arbitrary cross sections and the redundant work in the determination of the effective area for the sections with local buckling is no longer needed [28]. The elastic local buckling, global buckling and distortional buckling stress should be determined through the numerical analysis such as finite strip software CUFSM [28] or ABAQUS [36]. The non-dimensional slenderness parameter used in DSM and CSM is $(f_y/f_{cr})^{0.5}$, which is the same parameter used in AISI S100 [40] and AS/NZS 4600 [44]. The applicability of DSM for the design strength predictions for HSS IOctHS was also evaluated. For the sections with $\lambda_{lim}$ smaller than 1.47, those sections can achieve the yield load, and the cross-section yield limit from DSM is thereby taken as 1.47. Modified design method based on the DSM was proposed by Chen et al. [18] which aimed at deriving an updated expression for OctHS with strength grades varying from S235 to S690. The proposed yield limit value was 1.180 and this modified approach was named as DSM* in this study.

CSM, accounting for the strain hardening of the metallic material and the effect of the element interaction, is a deformation-based design method. Similar to the DSM that the iteration process of the effective area calculation of the cross section is not needed in the design of strength predictions [29, 45, 46]. To define the strain capacity of the cross section, different based curves were utilized in strength predictions for CSM. Currently, the base curve is only available for the commonly used tubular sections, such as SHS/RHS and CHS but not for the IOctHS investigated in this study. Hence, the applicability of the CSM for the design of the HSS IOctHS stub columns was evaluated. In terms of the material model, the material model for cold-formed structural steel section proposed by [1] was used for high strength steel. For HSS structural elements, base curve has been studied and developed for HSS based on the collated data from the tests under compressive in Lan et al. [47]. The based curve was thus employed in this study for flange, shown as follows in Eq. (4).

$$\begin{cases} \dfrac{\varepsilon_{csm}}{\varepsilon_y} = \dfrac{0.294}{\lambda_p^{3.174}} \le \min(15, \dfrac{C_1\varepsilon_u}{\varepsilon_y}) & \text{for } \lambda_p \le 0.68 \\ \dfrac{\varepsilon_{csm}}{\varepsilon_y} = (1 - \dfrac{0.219}{\lambda_p^{1.014}}) \dfrac{1}{\lambda_p^{1.014}} & \text{for } 0.68 < \lambda_p \end{cases} \quad (4)$$

where $(\varepsilon_{csm}/\varepsilon_y)$ is the deformation capacity, $\varepsilon_{csm}$ is the CSM limiting strain, $\varepsilon_y$ is the yield strain equals to $f_y/E$. For the sections subjected to local buckling prior to the achievement of the yield, the CSM provides a limit slenderness value of $\lambda_p = 0.68$, resulting in $\lambda_{lim} = 1.29$. Fig. 20 demonstrate that the yield slenderness limit from DSM, CSM as well as the one proposed from DSM* exhibit overly non-conservatism for the design of OctHS and IOctHS. The main findings of the assessment for cross-section yield slenderness limit are summarized herein, the comparisons between the limit value and the test data generally indicate that the codified slenderness limits in the three structural steel design standards of EN 1993-1-1, AISC 360-16 and AS 4100 cannot be applied to the cross-section classification of HSS cold-formed IOctHS stub columns under compression. Moreover, the cross-section yield slenderness limits from the design approaches of DSM, CSM, DSM* and CSM* result in over-predicted classification.

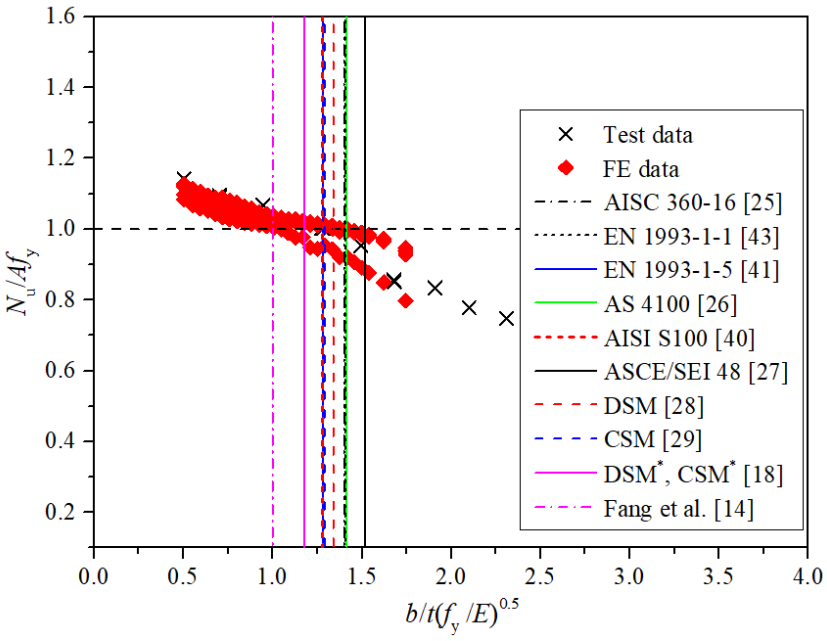


Fig. 20. Assessment of slenderness limits in the design codes and design approaches for HSS cold-formed IOctHS stub column in compression.

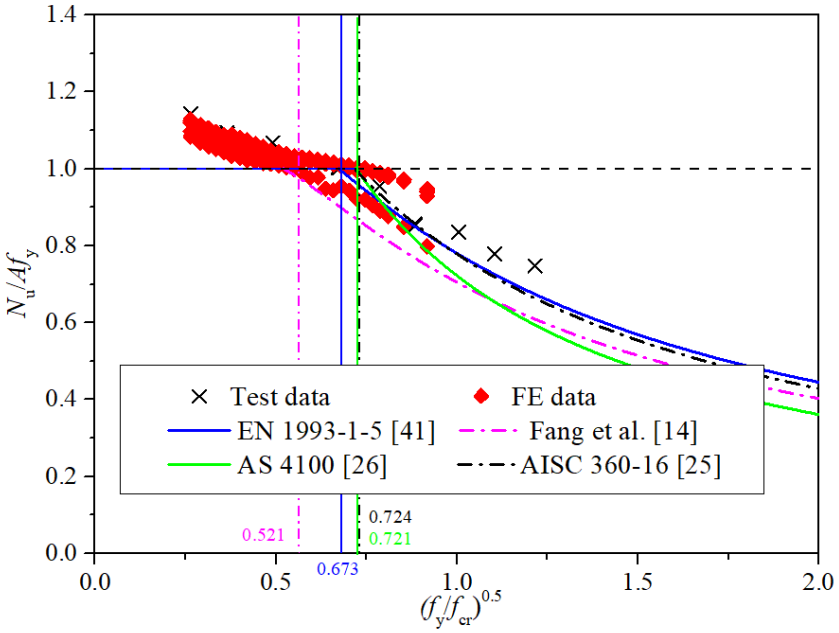


Fig. 21. Assessment of the effective width methods in design codes and design methods for HSS cold-formed IOctHS stub column in compression.

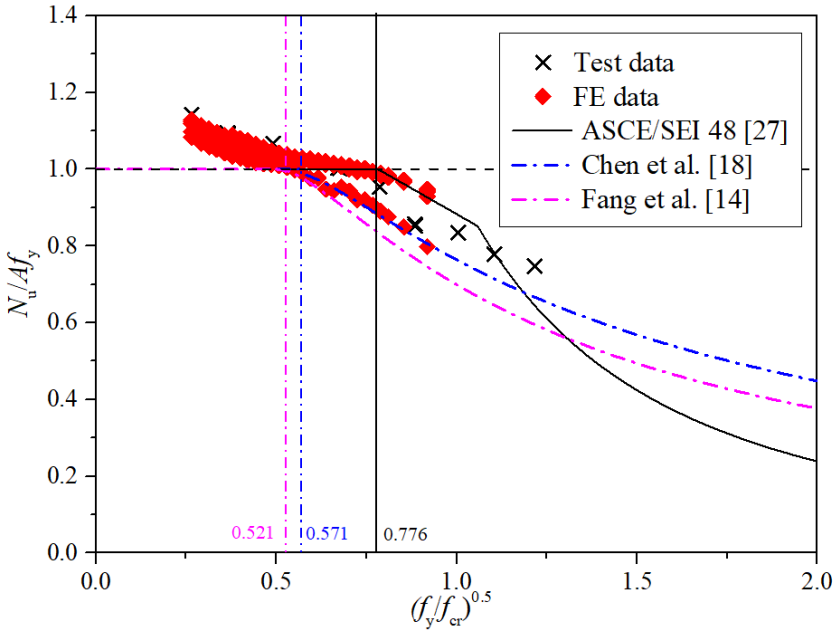


627

628 Fig. 22. Assessment of the design code of ASCE/SEI 48-11 and modified design methods based on it for HSS
629 cold-formed IOctHS stub column in compression.

630

631

632

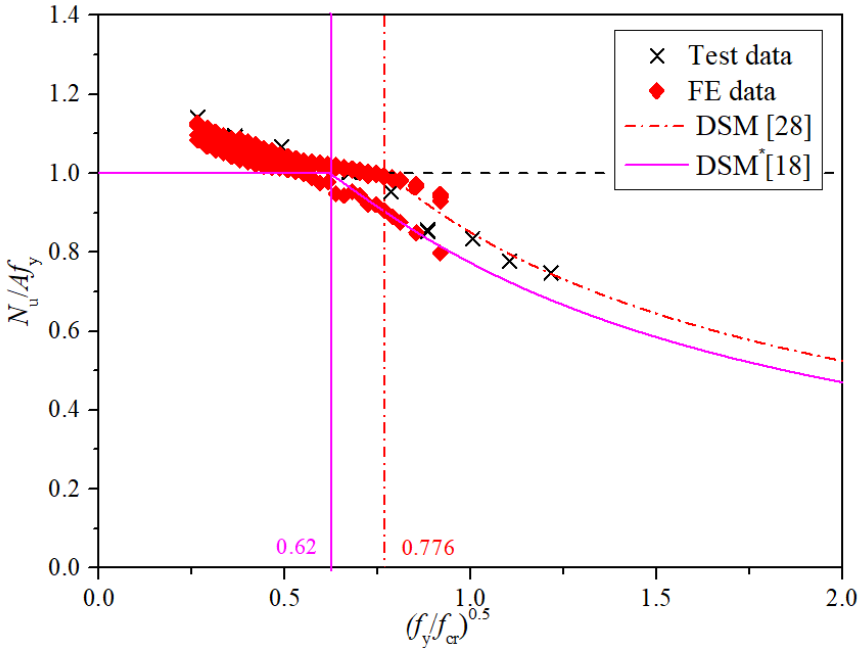


633

634 Fig. 23. Assessment of the DSM and DSM* for HSS cold-formed IOctHS stub column in compression.

635

636 Table 7 Summary of the cross-section yield slenderness limits for the internal plate element.

| Design standards and methods | Yield slenderness limits | $\lambda_{lim}$ |
|---|---|---|
| EN 1993-1-1 [43] | $b/t \leqslant 42\varepsilon_{EC3}$, $\varepsilon_{EC3}=\sqrt{235/f_y}$, $E = 210$ GPa | 1.405 |
| ANSI/AISC 360-16 [25] | $b/t \leqslant 1.40\varepsilon_{AISC}$, $\varepsilon_{AISC}=\sqrt{E/f_y}$, $E = 200$ GPa | 1.400 |
| EN 1993-1-5 [41] | $\overline{\lambda_p}=\frac{b/t}{28.4\varepsilon\sqrt{k}} \leq 0.5+\sqrt{0.085-0.055\psi}$, $\psi = 1$, $\varepsilon_{EC3}=\sqrt{235/f_y}$, $k = 4$, $E = 210$ GPa | 1.279 |
| AS 4100 [26] | $b/t \leqslant 14\varepsilon_{AS4100}$, $\varepsilon_{AS4100}=\sqrt{250/f_y}$, $E = 200$ GPa | 1.414 |
| ASCE/SEI 48-11 [27] | $b/t \leqslant 681.2/\sqrt{f_y}$, $E = 200$ GPa | 1.520 |
| AISI S100-16 [40]<br>AS/NZS 4600 [44] | $\lambda_p=\sqrt{f_y/f_{cr}} \leq 0.673$, $f_{cr}=4\frac{\pi^2 E}{12(1-\nu^2)}(\frac{t}{b})^2$, $E = 200$ GPa | 1.280 |
| DSM [28] | $\lambda_p=\sqrt{f_y/f_{cr}} \leq 0.776$, $E = 200$ GPa | 1.470 |
| CSM [29] | $\lambda_p=\sqrt{f_y/f_{cr}} \leq 0.68$, $E = 200$ GPa | 1.290 |
| DSM* [18] | $\lambda_p=\sqrt{f_y/f_{cr}} \leq 0.62$, $E = 200$ GPa | 1.180 |
| CSM* [18] | $\lambda_p=\sqrt{f_y/f_{cr}} \leq 0.62$, $E = 200$ GPa | 1.180 |
| Fang et al. [14] | $b/t \leqslant 30\varepsilon_{EC3}$, $\varepsilon_{EC3}=\sqrt{235/f_y}$, $E = 210$ GPa | 1.000 |
| ASCE/SEI 48-11* [18] | $\lambda_p=\sqrt{f_y/f_{cr}} \leq 0.521$, $E = 200$ GPa | 1.000 |

637

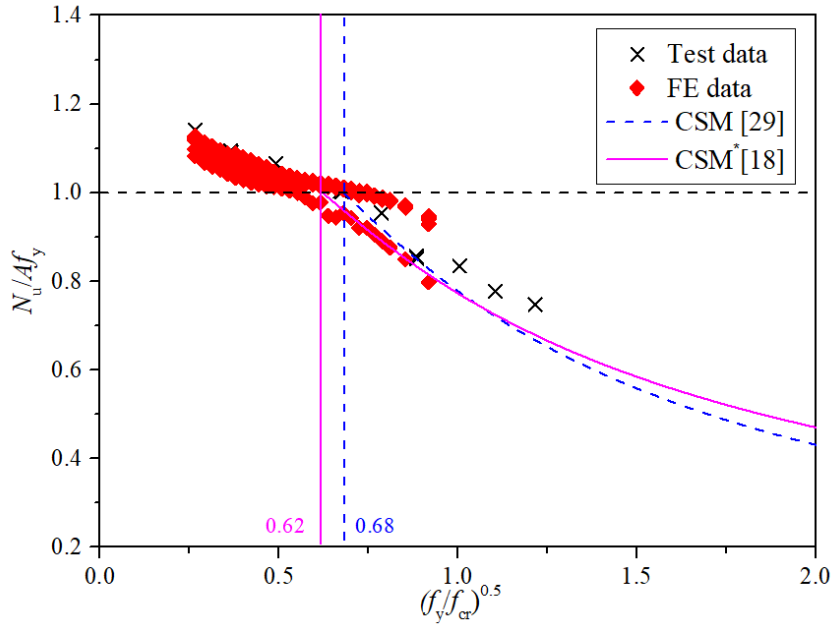


Fig. 24. Assessment of the CSM and CSM* for HSS cold-formed IOctHS stub column in compression.

5.3 Cross-section compression resistances

5.3.1 Design standards and modified methods

Brief introduction on cross-section strength predictions under compression from the design standards and the design methods are given in this section. As discussed in sub-section of 5.1 and 5.2, for the cross sections of the structural elements experienced local buckling failure prior to the attainment of yielding, the effective width method is employed in current design codes in EN 1993-1-5 [41] and ANSI/AISC 360-16 [25] and AS 4100 [26]. It should be noted that the EN 1993-1-12, ANSI/AISC 360-16, and AS 4100 employ different equations to determine the effective width of the plate elements of Class 4 or slender section subject to local buckling, as given in Eqs. (5) – (8)

$$\frac{b_{\text{eff,EC3}}}{b}=\begin{cases}1 & \text{for } \overline{\lambda}_{\text{p}}\le 0.673\\ \left(1-0.22/\overline{\lambda}_{\text{p}}\right)/\overline{\lambda}_{\text{p}} & \text{for } \overline{\lambda}_{\text{p}}>0.673\end{cases} \tag{5}$$

where $\overline{\lambda}_{\text{p}}$ is the plate slenderness specified in accordance with EN 1993-1-5 [38], as shown in Eq. (6).

$$\overline{\lambda}_{\text{p}}=\frac{b/t}{28.4\varepsilon_{\text{EC3}}\sqrt{k_{\sigma}}} \tag{6}$$

where $k_{\sigma}$ is the buckling factor taken as 4 for internal plate element in compression.

The equations to determine the effective width in structural steel design codes of ANSI/AISC 360-16 [25] and AS 4100 [26] are given in Eq. (7) and Eq. (8), respectively.

$$\frac{b_{\text{eff,AISC}}}{b}=\frac{1.38\lambda_{\text{p,AISC}}}{\lambda}-\frac{0.38\lambda_{\text{p,AISC}}{}^{2}}{\lambda^{2}} \tag{7}$$

where $\lambda_{\text{p,AISC}}$ is the AISC limiting width-to-thickness ratio for internal plate element under compression and $\lambda$ is the ratio of width to thickness $b/t$.

$$\frac{b_{\text{eff,AS4100}}}{b}=\frac{40}{b/(t\varepsilon_{\text{AS4100}})} \tag{8}$$

It should be noted that design standard of ASCE/SEI 48-11 [27] adopts effective strength to consider the reduced capacity due to local buckling, as follows in Eq. (9)

$$f_{\text{a,ASCE}}=\begin{cases} f_{\text{y}} & \text{for } \dfrac{b}{t}\le\dfrac{681.2}{\sqrt{f_{\text{y}}}} \\ 1.42f_{\text{y}}\left(1-\dfrac{0.00114}{2.62}\dfrac{b\sqrt{f_{\text{y}}}}{t}\right) & \text{for } \dfrac{681.2}{\sqrt{f_{\text{y}}}}\le\dfrac{b}{t}\le\dfrac{919.6}{\sqrt{f_{\text{y}}}} \\ 4\dfrac{\pi^{2}E}{12(1-\nu^{2})}\left(\dfrac{t}{b}\right)^{2} & \text{for } \dfrac{919.6}{\sqrt{f_{\text{y}}}}\le\dfrac{b}{t} \end{cases} \tag{9}$$

where $A$ is the gross cross-section area, $f_{\text{a,ASCE}}$ is the effective compressive strength, $f_{\text{y}}$ is the yield strength and $b$ is the clear side width excluding corner portion.

Applicability of the existing EWM was assessed for HSS OctHS in Fang et al. [14], it is found that the EWM in EN 1993-1-5 [41] over-estimated the cross-section strength and EWM was modified and proposed as follows in Eq. (10) in a form analogous to the expression given in EN 1993-1-5 [41]. The cross-section predictions based on the modified method was named as $N_{\text{u,Fang}}$.

$$\frac{b_{\text{eff,EC3}}}{b}=\begin{cases} 1 & \text{for } \overline{\lambda_{\text{p}}}\le 0.521 \\ \left(0.905-0.2/\overline{\lambda_{\text{p}}}\right)/\overline{\lambda_{\text{p}}} & \text{for } \overline{\lambda_{\text{p}}}>0.521 \end{cases} \tag{10}$$

Along with the modified EWM, reduced strength method based on ASCE/SEI 48-11 [27] was also proposed as follows, based on the updated strength, the cross-section capacity was defined as $N_{\text{u,ASCE}}{}^{*}$.

$$f_{\text{a,ASCE}}{}^{*}=\begin{cases} f_{\text{y}} & \text{for } \overline{\lambda_{\text{p}}}\le 0.521 \\ f_{\text{y}}\left(0.9-\dfrac{0.21}{\overline{\lambda_{\text{p}}}^{1.1}}\right)\dfrac{1}{\overline{\lambda_{\text{p}}}^{1.1}} & \text{for } \overline{\lambda_{\text{p}}}>0.521 \end{cases} \tag{11}$$

Likewise, the modified reduced strength method was also proposed in [18] as follows, resulting cross-section resistance of $N_{\text{u,ASCE}}{}^{\#}$.

$$f_{\text{a,ASCE}}{}^{\#}=\begin{cases} f_{\text{y}} & \text{for } \overline{\lambda_{\text{p}}}\le 0.571 \\ f_{\text{y}}\left(1.05-\dfrac{0.276}{\overline{\lambda_{\text{p}}}}\right)\dfrac{1}{\overline{\lambda_{\text{p}}}} & \text{for } \overline{\lambda_{\text{p}}}>0.571 \end{cases} \tag{12}$$

688
689 5.3.2 Design approaches of DSM and CSM
690
691 As introduced in the previous section that DSM adopted cross-section slenderness limit $\lambda_p$. For the structural
692 members with cross-section slenderness limit $\lambda_p < 0.776$, yield load can be achieved, for those sections with
693 cross-section slenderness limit $\lambda_p \geq 0.776$, the predicted strength could be determined following the equation
694 expressed by Eq. (13).
695

696
$$N_{DSM} = \begin{cases} f_y A & \text{for } \lambda_p \leq 0.776 \\ 1 - \frac{0.15}{\lambda_p^{0.8}} \frac{1}{\lambda_p^{0.8}} f_y A & \text{for } \lambda_p > 0.776 \end{cases} \quad (13)$$

697
698 Chen et al. [18] concluded that DSM generated over-conservative strength predictions for OctHS with strength
699 grades varied from S235 and S690, modified coefficients were applied to the design equation as shown in Eq.
700 (14).

701
$$N_{DSM}^{*} = \begin{cases} f_y A & \text{for } \lambda_p \leq 0.62 \\ 1 - \frac{0.227}{\lambda_p^{0.9}} \frac{1}{\lambda_p^{0.9}} f_y A & \text{for } \lambda_p > 0.62 \end{cases} \quad (14)$$

702 In terms of the cross-section strength predictions from CSM, the CSM limiting stress $f_{csm}$, strain hardening
703 slope $E_{sh}$ and the predicted strain $\varepsilon_u$ corresponding to the ultimate stress are needed. The CSM limiting stress
704 $f_{csm}$ can be calculated from Eq. (15),
705

706
$$f_{csm} = \begin{cases} E_s \varepsilon_{csm} & \text{for } \varepsilon_{csm} \leq \varepsilon_y \\ f_y + E_{sh}(\varepsilon_{csm} - \varepsilon_{sh}) & \text{for } \varepsilon_y < \varepsilon_{csm} < C_1 \varepsilon_u \end{cases} \quad (15)$$

707
708 where $E_s$ is Young's modulus, $f_y$ is the yield stress, $\varepsilon_y$ and $\varepsilon_u$ are the strains at the yield and ultimate stresses,
709 respectively, $\varepsilon_{sh}$ is the strain hardening strain defined as the end of the yield plateau after which the strain
710 hardening initiates, $C_1\varepsilon_u$ represents the strain at the intersection point of the third stage of the model and the
711 actual stress-strain curve. Moreover, material coefficients, $C_1$ used in the material model defining cut-off strain
712 to avoid over-predictions of material strength. The other material coefficients $C_2$ is used to define the strain
713 hardening modulus of $E_{sh}$, as given in Eq. (16). These material coefficients corresponding to the material
714 properties in this study were derived with regard to the proposed material model proposed in [1] for HSS with
715 extensive materials collated.
716

717
$$E_{sh} = \frac{f_u - f_y}{C_2 \varepsilon_u - \varepsilon_y} \quad (16)$$

718 After determining the CSM limiting stress, the cross-section strength can be derived as follows,
719

$$N_{csm} = \begin{cases} f_{csm} A & \text{for } \lambda_p \le 0.68 \\ \dfrac{\varepsilon_{csm}}{\varepsilon_y} f_y A & \text{for } \lambda_p > 0.68 \end{cases} \quad (17)$$

Note that the modified CSM* proposed in Chen et al. [18] simply extended the modified expressions of DSM* for the sections with $\lambda_p \ge 0.62$. The suitability of this modified CSM* to HSS cold-formed IOctHS was also evaluated and compared.

5.3.3 Assessment of the applicability of the existing design methods

The ultimate loads obtained from the experiments in conjunction with the FE data were compared with the strength predictions based on design codes and design methods introduced in sub-sections of 5.3.1 and 5.3.2. The test results were normalized with the strength predictions and normalized strength ratios are plotted against the corresponding cross-sectional slenderness $\lambda_p$ with all partial factors set to unity for direct comparison, as shown in Figs. 25–27.

Key test results with the statistical analysis and comparisons of the cross-section resistance predictions, including the mean (test and FE)-to-predicted compression resistance ratios $N_u/N_{u,pred}$, the corresponding coefficient of variations (CoVs), are shown in Table 8. Strength predictions from three structural steel design codes and the proposed method in Fang et al. [14] were based on the concept of EWM. Hence the comparisons among these three design codes and one modified method were carried out. The mean values of $N_u/N_{u,pred}$ obtained from EN 1993-1-12, AISC 360-16, AS4100 and Fang et al. [14] are 1.03, 1.02, 1.03 and 1.05 with corresponding CoVs of 0.043, 0.048, 0.042 and 0.031 respectively. As seen in Fig. 25, for the relatively compact sections, design codes as well as modified EWM both provide over-conservative results and over-predicted cross-section strengths were observed from the existing design standards for slender sections, as seen in Fig. 21. Three structural steel design codes give consistent predictions, and AISC 360-16 generally provide close predictions on average but more scattered. Modified EWM provides comparably reliable and safe predictions for HSS cold-formed IOctHS under compression, as shown in Fig. 25.

In terms of the comparisons based on the standard of ASCE/SEI 48-11 and modified methods in Fang et al. [14] and Chen et al. [18], the mean values of $N_u/N_{u,pred}$ are 1.02, 1.05 and 1.04 with corresponding CoVs of 0.052, 0.031 and 0.039 respectively. Though relative accurate predictions were obtained from ASCE/SEI 48-11 [27], it over-estimated the strength for slender sections significantly, as shown in Fig. 26. The extent of the over-prediction tends to increase as the cross-section slenderness increasing. Modified methods proposed by Fang et al. [14] and Chen et al. [18] based on reduced strength method (ASCE/SEI 48-11 [27]) provide reliable and accurate predictions though all of which under-estimate the cross-section strength for compact sections. Compared with predictions from Fang et al. [14], the design equations in Chen et al. [18] gives non-conservative predictions for the sections with cross-section slenderness $\lambda_p$ ranging between 0.5 and 0.6. Design equations proposed in Fang et al. [14] provide more reliable results and suitable cross-section yield slenderness value, as shown in Fig. 22.

Regarding the strength predictions from the design methods of DSM, CSM and modified design methods of DSM* and CSM*, normalized strengths are plotted against the cross-section slenderness $\lambda_p$ in order to assess

the design equations of DSM and DSM*, as shown in Fig. 23. The mean values of $N_u/N_{u,pred}$ obtained from DSM and DSM* are 1.03 and 1.06 with CoVs of 0.045 and 0.030 respectively and the mean values of $N_u/N_{u,pred}$ obtained from CSM and CSM* are 1.04 and 1.04 with CoVs of 0.025 and 0.030 respectively. It is noticeable that DSM significantly over-estimates the cross-section strength with design equation locating as the lower bound of the IOctHS with aspect ratio of 2.0. In comparison with DSM, DSM* can be able to provide more reliable predictions, notwithstanding cross-section strengths are still slightly over-estimated with slenderness $\lambda_p$ between 0.62 and 0.65. Furthermore, both DSM and DSM* give over-conservative cross-section predictions for compact sections, as shown in Fig. 27. Likewise, assessment of the prediction equation of CSM and CSM* were conducted against the test and FE data. It is seen that both design curves of CSM and CSM* locate above the data point exhibiting conservatism predictions, as shown in Fig. 24. Fig. 27 implies that CSM and CSM* provide more consistent and precise predictions than DSM and DSM*. In particular, accurate strength predictions for compact sections were obtained due to that CSM can take strain hardening of the material into account. Though CSM* determine more accurate predictions for compact sections than CSM, it starts to underestimate the strength as cross-section slenderness limits increasing.

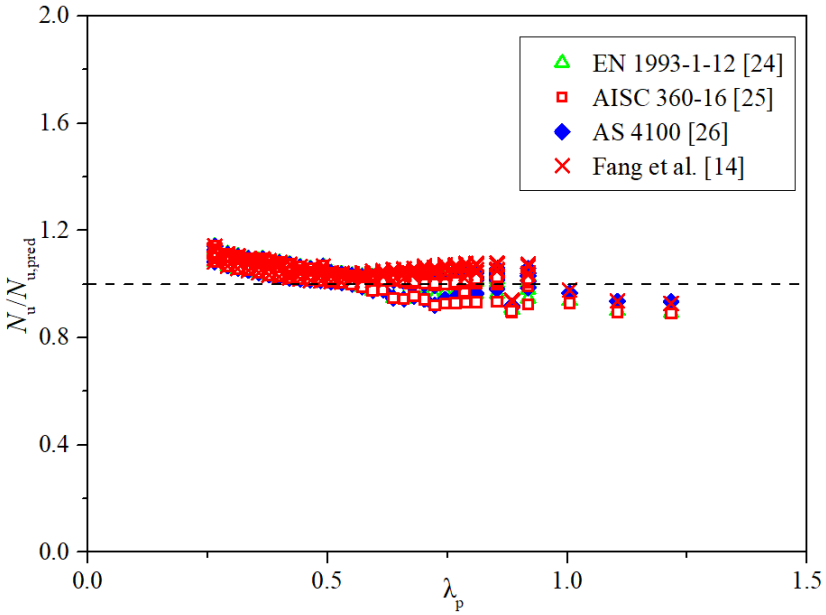


Fig. 25. Comparisons of experimental and numerical results with strength predictions from design codes and design approach using effective width method.

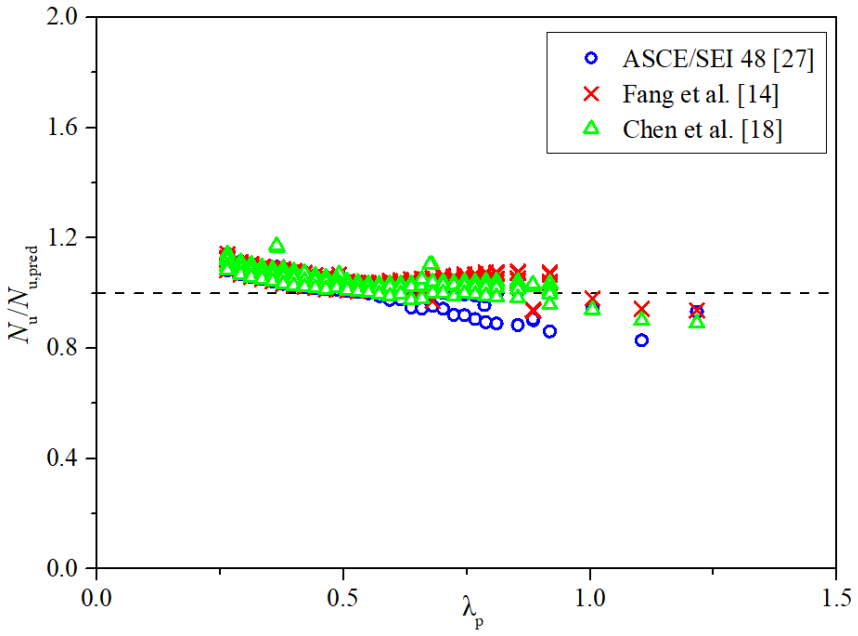


Fig. 26. Comparisons of experimental and numerical results with strength predictions from design code of ASCE/SEI 48-11 and modified design approaches based on ASCE/SEI 48-11.

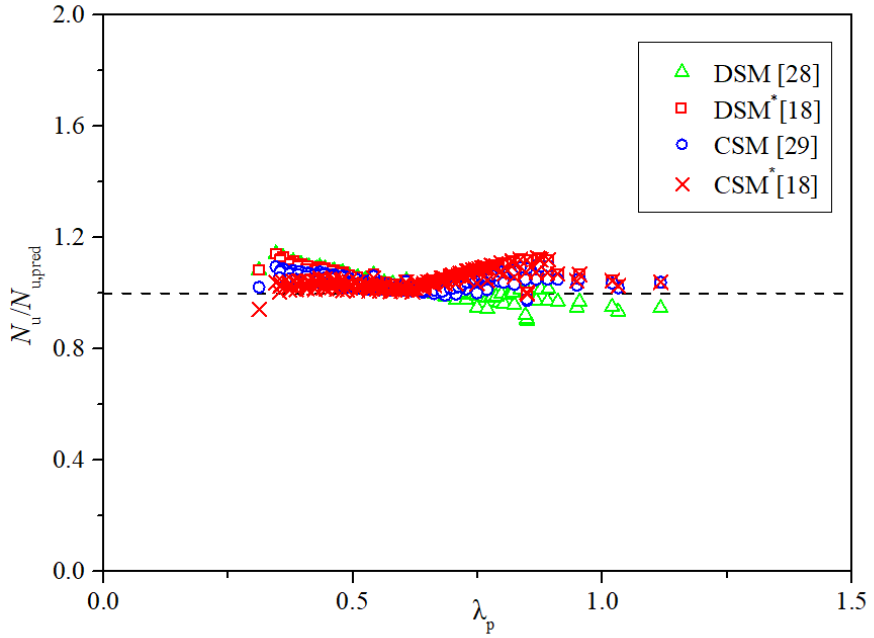


Fig. 27. Comparisons of experimental and numerical results with strength predictions from design approaches of DSM and CSM as well as the modified design approaches DSM* and CSM*.

## 6. Reliability analysis

The first-order reliability method in accordance with EN 1990 [48] was conducted to assess the reliability level of the design codes and design methods on HSS cold-formed IOctHS stub columns. The material over-strength

ratio $f_{y,mean}/f_{y,nom}$ = 1.12 proposed in Chen et al. [1] for HSS was used with CoV of 0.066. The CoV of the geometric properties was taken as 0.05 [49]. The key reliability analysis results are shown in Table 8. In this table, $b$ is the mean value correction factor, which can be derived based on least squares analysis between the resistance capacities and design predictions, where $r_e$ is the experimental results and $r_t$ is the theoretical results of the resistance model.

$$b = \frac{\sum r_e r_t}{\sum r_t^2} \tag{18}$$

$V_\delta$ is the CoV of the test and FE results relative to the resistance design model, which can be determined as follows, in Eqs. (19) – (21).

$$V_\delta = \sqrt{\exp(s_\Delta^{\,2}) - 1} \tag{19}$$

$$s_\Delta^{\,2} = \frac{1}{n-1}\sum_{i=1}^{n}(\Delta_i - \frac{1}{n}\sum_{i=1}^{n}\Delta_i)^2 \tag{20}$$

$$s_\Delta^{\,2} = \ln(\delta_i) \tag{21}$$

where δ is the error term which is calculated for each pair data $\delta = r_e / b\, r_t$.

The effect of the variability of the geometric and material in resistance function $g_{rt}(X)$ are accounted for through their coefficient of variation parameter $V_{rt}$. The calculation of this parameter is shown in Eq. (22)

$$V_{rt} = \frac{VAR\left[g_{rt}(\underline{X})\right]}{g_{rt}^{\,2}(\underline{X}_m)} \cong \frac{1}{g_{rt}^{\,2}(\underline{X}_m)} \times \sum_{i=1}^{j}(\frac{\partial g_{rt}}{\partial X_i}\sigma_i)^2 \tag{22}$$

$V_r$ is the combined CoV incorporating both model and basic variable uncertainties, and $\gamma_{M0}$ is the partial safety factor for cross section resistance. To determine the partial safety factor, design resistance value needs to be derived as follows,

$$r_d = b g_{rt}(\underline{X}_m)\exp(-k_{d,\infty}\alpha_{rt}Q_{rt} - k_{d,n}\alpha_\delta Q_\delta - 0.5Q^2) \tag{23}$$

where $\alpha_{rt} = Q_{rt}/Q$, $\alpha_\delta = Q_\delta/Q$, $Q_{rt} = \sqrt{\ln(V_{rt}^{\,2}+1)}$, $Q_\delta = \sqrt{\ln(V_\delta^{\,2}+1)}$, and $Q = \sqrt{\ln(V_r^{\,2}+1)}$.

Based on the statistical results in Table 8, it was concluded that the examined design standards and design methods provide comparative accurate predictions with mean (test and FE)-to-predicted between 1.02 and 1.06. The required partial factors are summarized in Table 8 for the design standards and design methods discussed in the previous sections, which are larger than the value of 1.0 recommended in EN 1993-1-1 [43] and EN 1993-1-5 [41].

## 7. Conclusions

Experimental and numerical investigations on the local buckling behaviour and cross-section capacity under compression was performed for high strength steel Q690 IOctHS with press-braking corners and the aspect ratios of the examined sections were within range between 1.0 and 2.0. The applicability of the yield slenderness limits for cross-section classification for HSS cold-formed IOctHS in compression and design rules specified in structural steel design codes and the transmission pole code were assessed and discussed. The cross-section strength predictions obtained from the design standards and design approaches were compared with the test data and FE results. Reliability analysis was also carried out. Base on the results and discussions presented in this paper, the following conclusions can be drawn and briefly summarized as follows:

(a) The codified slenderness limits in the three structural steel design standards of EN 1993-1-1, AISC 360-16 and AS 4100 cannot be extended to cover the cross-section classification of HSS cold-formed IOctHS stub columns under compression.

(b) The cross-section yield slenderness limits from DSM, CSM, DSM* and CSM* both provide non-conservative predictions.

(c) Three structural steel design standards provide relatively consistent and accurate results. The compact sections strength are under-estimated and slender sections are over-estimated by three design standards, while the modified method proposed by Fang et al. provide more reliable and safe predictions than the standards.

(d) Modified strength reduced method proposed by Fang et al. [14] yield more accurate and reliable design than the one proposed by Chen et al. [18]. Chen et al. [18] somewhat under-estimate the strength with cross-sections slenderness $\lambda_p$ varying between 0.5 and 0.6.

(e) DSM* can provide more reliable predictions than DSM, though many data point are still over-estimated. DSM design curve exhibits overly non-conservatism. For compact sections, both DSM and DSM* yield under-estimated results as the strain hardening of the material cannot be accounted for.

(f) CSM and CSM* provide more consistent and precise results than the methods of DSM and DSM*, satisfactorily predicted results for compact sections are given from both CSM and CSM*. Compared with CSM, the modified CSM* is more precise in determine the compact sections' strength but showing drawbacks in predicting the cross-section strength with larger cross-section slenderness.

Though cross-section strength predictions are provided by modified approaches, conservative results are still observed for the sections with higher aspect ratio. For the purpose of simplicity, the modified approaches can be applied to HSS cold-formed IOctHS design in practice. But to improve the efficiency of structural steel design, design methods and effective width equations stipulated in those design codes, should be further investigated focusing on the respective aspect ratio, which is currently under way.

Table 8 Comparisons of test and FE results with predicted strengths based on different design methods.

| Number of Specimen | | $N_{u,test}$ /$N_{u,EC3}$ | $N_{u,test}$ /$N_{u,AISC}$ | $N_{u,test}$ /$N_{u,AS4100}$ | $N_{u,test}$ /$N_{u,DSM}$ | $N_{u,test}$ /$N_{u,DSM}^{*}$ | $N_{u,test}$ /$N_{u,CSM}$ | $N_{u,test}$ /$N_{u,CSM}^{*}$ | $N_{u,test}$ / $N_{u,ASCE}$ | $N_{u,test}$ / $N_{u,Fang}$ | $N_{u,test}$ /$N_{u,ASCE}^{*}$ | $N_{u,test}$ /$N_{u,ASCE}^{\#}$ |
|---|---|---|---|---|---|---|---|---|---|---|---|---|
| Test:13 | FE:140 | | | | | | | | | | | |
| | Mean | 1.03 | 1.02 | 1.03 | 1.03 | 1.06 | 1.04 | 1.04 | 1.02 | 1.05 | 1.05 | 1.04 |
| | CoV | 0.043 | 0.048 | 0.042 | 0.045 | 0.030 | 0.025 | 0.030 | 0.052 | 0.031 | 0.031 | 0.039 |
| | $k_{d,n}$ | 3.157 | 3.157 | 3.157 | 3.157 | 3.157 | 3.157 | 3.157 | 3.157 | 3.157 | 3.157 | 3.157 |
| | $b$ | 1.009 | 1.002 | 1.011 | 1.006 | 1.059 | 1.036 | 1.049 | 0.994 | 1.043 | 1.040 | 1.026 |
| | $V_{\delta}$ | 0.044 | 0.048 | 0.042 | 0.047 | 0.030 | 0.025 | 0.030 | 0.053 | 0.031 | 0.032 | 0.039 |
| | $V_{r}$ | 0.094 | 0.096 | 0.093 | 0.095 | 0.088 | 0.087 | 0.088 | 0.098 | 0.088 | 0.088 | 0.092 |
| | $\gamma_{M0}$ | 1.15 | 1.15 | 1.14 | 1.18 | 1.11 | 1.13 | 1.12 | 1.18 | 1.13 | 1.13 | 1.14 |

## Data Availability Statement

Some or all data that support the findings of this study are available from the corresponding author upon reasonable request.

## Acknowledgement

The research work presented in this paper was supported by a grant from the Research Grants Council of the Hong Kong Special Administrative Region, China (Project no. 15218918). The authors would also like to thank the technical staff, Mr. H.Y. Leung, Mr. K.H. Wong, Mr. K.L. Cheung of the Structural Engineering Research Laboratory for their support as well as the support from the Industrial Center at The Hong Kong Polytechnic University.

## References

[1] S. Chen, H. Fang, J.-z. Liu, T.-M. Chan, Design for local buckling behaviour of welded high strength steel I-sections under bending, Thin-Walled Struct. 172 (2022) 108792.
[2] J.-Z. Liu, H. Fang, S. Chen, T.-M. Chan, Material properties and residual stresses of high strength steel hexagonal hollow sections, J. Constr. Steel. Res. 190 (2022) 107061.
[3] T. Usami, Y. Fukumoto, Local and overall buckling of welded box columns, J. Struct. Div. 108(3) (1982) 525-542.
[4] K.J.R. Rasmussen, G.J. Hancock, Plate slenderness limits for high strength steel sections, J. Constr. Steel. Res. 23 (1992) 73-96.
[5] G. Shi, W. Zhou, Y. Bai, C. Lin, Local buckling of 460 MPa high strength steel welded section stub columns under axial compression, J. Constr. Steel. Res. 100 (2014) 60-70.
[6] N. Schillo, M. Feldmann, Interaction of local and global buckling of box sections made of high strength steel, Thin-Walled Struct. 128 (2018) 126-140.
[7] J.-L. Ma, T.-M. Chan, B. Young, Experimental Investigation on Stub-Column Behavior of Cold-Formed High-Strength Steel Tubular Sections, J. Struct. Eng. 142(5) (2016) 04015174.
[8] J.-L. Ma, T.-M. Chan, B. Young, Cold-formed high strength steel tubular beam-columns, Eng. Struc. 230 (2021) 111618.
[9] H. Fang, T.M. Chan, B. Young, Structural performance of cold-formed high strength steel tubular columns, Eng. Struc. 177 (2018) 473-488.
[10] H. Fang, T.M. Chan, Resistance of Axially Loaded Hot-finished S460 and S690 Steel Square Hollow Stub Columns at Elevated Temperatures, Structures 17 (2018) 66-73.
[11] J. Wang, S. Afshan, N. Schillo, M. Theofanous, M. Feldmann, L. Gardner, Material properties and compressive local buckling response of high strength steel square and rectangular hollow sections, Eng. Struc. 130 (2017) 297-315.
[12] M. Gkantou, M. Theofanous, J. Wang, C. Baniotopoulos, L. Gardner, Behaviour and design of high-strength steel cross-sections under combined loading, Proc. Inst. Civil Eng.-Struct. Build. 170(11) (2017) 841-854.
[13] P.S. Bulson, The strength of the thin-walled tubes formed from flat elements, Int. J. Mech. Sci. 11 (1969) 613-620.
[14] H. Fang, T.-M. Chan, B. Young, Behavior of Octagonal High-Strength Steel Tubular Stub Columns, J.

Struct. Eng. 145(12) (2019) 04019150.
[15] H. Fang, T.-M. Chan, B. Young, Experimental and Numerical Investigations of Octagonal High-Strength Steel Tubular Stub Columns under Combined Compression and Bending, J. Struct. Eng. 147(1) (2021) 04020282.
[16] H. Fang, T.-M. Chan, B. Young, Structural performance of concrete-filled cold-formed high-strength steel octagonal tubular stub columns, Eng. Struc. 239 (2021) 112360.
[17] J.B. Chen, J.Y. Zhu, T.M. Chan, Experimental and numerical investigation on stub column behaviour of cold-formed octagonal hollow sections, Eng. Struc. 214 (2020) 110669.
[18] J. Chen, H. Fang, T.-M. Chan, Design of fixed-ended octagonal shaped steel hollow sections in compression, Eng. Struc. 228 (2021) 111520.
[19] J.Z. Liu, H. Fang, T.M. Chan, Experimental investigation on material properties and residual stresses in cold-formed high strength steel irregular octagonal hollow sections, J. Constr. Steel. Res. 191 (2022) 107170.
[20] Z.M. Dalia, A.K. Bhowmick, G.Y. Grondin, Local buckling of multi-sided steel tube sections under axial compression and bending, J. Constr. Steel. Res. 186(4) (2021) 106909.
[21] J.S. Kabanda, Comparison of the moment rotation capacities of rectangular and polygonal hollow sections, J. Constr. Steel. Res. 137 (2017) 66-76.
[22] J-Z. Liu, H Fang, T-M Chan. Investigations on material properties and residual stresses in cold-formed high strength steel irregular hexagonal hollow sections. Thin-Walled Struct. 2022; 175: 109220.
[23] J-Z. Liu, H Fang, T-M Chan. Experimental investigations on material properties and stub column behaviour of high strength steel irregular hexagonal hollow sections. J. Constr. Steel. Res. (2022) 107343. (in publication)
[24] EN 1993-1-12, Eurocode 3: Design of Steel Structures – Part 1–12: Additional Rules for the Extension of EN 1993 up to Steel Grades S700, European Committee for Standardization (CEN), Brussels, 2007.
[25] ANSI/AISC 360-16, Specification for Structural Steel Buildings, American Institute of Steel Construction (AISC), Chicago, 2016.
[26] AS 4100-1998(R2016), Steel structures (Reconfirmed 2016 Incorporating Amendment No.1), AS 4100, Australian Standard, Sydney, Australia, 2016.
[27] ASCE/SEI 48-11, Design of steel transmission pole structures, American Society of Civil Engineers, Reston, Virginia, 2011.
[28] B.W. Schafer, Review: The Direct Strength Method of cold-formed steel member design, J. Constr. Steel. Res. 64(7-8) (2008) 766-778.
[29] L. Gardner, D.A. Nethercot, Structural stainless steel design: A new approach, Structural Engineer 82(21) (2004) 21-28.
[30] EN ISO 6892-1, Metallic Materials – Tensile Testing Part 1: Method of Test at Ambient Temperature, EN ISO 6892-1, CEN, Brussels, Belgium, 2019.
[31] EN 1993-1-8, Eurocode 3: Design of steel structures - Part 1-8: Design of joints European Committee for Standardization (CEN), Brussels, 2005.
[32] J. Chen, T.-M. Chan, A.H. Varma, Stub Column Behavior of Cold-Formed High-Strength Steel Circular Hollow Sections under Compression, J. Struct. Eng. 146(12) (2020) 04020277.
[33] J-Z. Liu, S. Chen, T-M. Chan, Testing, numerical modelling and design of Q690 high strength steel welded T-section stub columns. Eng Struc. 259 (2022) 114142.
[34] J-Z. Liu, S. Chen, T-M. Chan, Experimental and numerical investigations of hybrid high-strength steel welded T-section stub columns with Q690 flange and Q460 web. Thin-Walled Struct. (2022) 109403. (in publication)

[35] R.D. Ziemian, Guide to stability design criteria for metal structures, John Wiley & Sons2010.
[36] ABAQUS/Standard. Version 6.14-1, K. a. S. Hibbit, U.S.A.
[37] T.M. Chan, L. Gardner, Bending strength of hot-rolled elliptical hollow sections, J. Constr. Steel. Res. 64(9) (2008) 971-986.
[38] T.M. Chan, L. Gardner, Flexural Buckling of Elliptical Hollow Section Columns, J. Struct. Eng. 135(5) (2009) 546-557.
[39] J.L. Ma, T.M. Chan, B. Young, Design of Cold-Formed High-Strength Steel Tubular Stub Columns, J. Struct. Eng. 144(6) (2018) 04018063.
[40] AISI S100-16, North American Specification for the Design of Cold-Formed Steel Structural Members, AISI (American Iron and Steel Institute), Washington, DC, USA, 2016.
[41] EN 1993-1-5, Eurocode 3: Design of Steel Structures – Part 1–5: Plated structural elements., European Committee for Standardization (CEN), Brussels, 2006.
[42] J.Y. Zhu, T.M. Chan, B. Young, Cross-sectional capacity of octagonal tubular steel stub columns under uniaxial compression, Eng. Struc. 184 (2019) 480-494.
[43] EN 1993-1-1, Eurocode 3: Design of Steel STRUCTURES – Part 1.1: General Rules and Rules for Buildings, European Committee for Standardization (CEN), Brussels, 2005.
[44] AS/NZS 4600:2018, Cold-formed steel structures, AS/NZS 4600, Australian/New Zealand Standards, Sydney, Australia and Wellington, New Zealand, 2018.
[45] C. Buchanan, L. Gardner, A. Liew, The continuous strength method for the design of circular hollow sections, J. Constr. Steel. Res. 118 (2016) 207-216.
[46] X. Yun, L. Gardner, N. Boissonnade, The continuous strength method for the design of hot-rolled steel crosssections, Eng. Struc. 157 (2018) 179-191.
[47] X. Lan, J. Chen, T.-M. Chan, B. Young, The continuous strength method for the design of high strength steel tubular sections in compression, Eng. Struc. 162 (2018) 177-187.
[48] EN 1990. Eurocode - Basis of structural design, European Committee for Standardization (CEN), Brussels, Belgium, 2002.
[49] S. Afshan, P. Francis, N.R. Baddoo, L. Gardner, Reliability analysis of structural stainless steel design provisions, J. Constr. Steel. Res. 114 (2015) 293-304.